Longitudinal, simultaneous wide-field fluorescent Ca^{2+} imaging and fMRI in awake mice

Francesca Mandino[1,2*], Taekyung Kang[3], Xilin Shen[1], Corey Horien[4], Xenophon Papademetris[1,2,3,5,6], Stephen M Strittmatter[6,7,8,9,10], Evelyn MR Lake[1,2,3,6*]

*Correspondence: francesca.mandino@yale.edu & evelyn.lake@yale.edu

[1]Department of Radiology and Biomedical Imaging, Yale School of Medicine, New Haven, CT, 06520, USA.
[2] Biomedical Imaging Institute, Yale University, New Haven, CT, 06511, USA.
[3]Department of Biomedical Engineering, Yale University, New Haven, CT, 06511, USA.
[4]Department of Psychiatry, University of Pennsylvania, Philadelphia, PA, 19104, USA.
[5]Department of Biomedical Informatics & Data Science
[6]Wu Tsai Institute, Yale University School of Medicine, New Haven, CT 06510, USA.
[7]Cellular Neuroscience, Neurodegeneration and Repair Program, Yale School of Medicine, New Haven, CT, 06520, USA.
[8]Department of Neurology, Yale University School of Medicine, New Haven, CT 06510, USA.
[9]Kavli Institute of Neuroscience, Yale University School of Medicine, New Haven, CT 06510, USA.
[10]Department of Neuroscience, Yale University School of Medicine, New Haven, CT 06510, USA.

Keywords. Awake, mouse, functional magnetic resonance imaging, blood oxygen level-dependent signal, multimodal imaging, wide-field imaging, fluorescent calcium imaging, functional connectivity, brain networks

Abstract. Functional magnetic resonance imaging (fMRI) can be applied in mice and humans making it a key technology in translational neuroimaging research. Yet, most neuroimaging studies in rodents use anesthesia to limit subject motion and stress. This puts a hard boundary on the range of brain and behavioral states that can be studied in animals, and deviates from the near-universal practice of imaging people whilst awake. Recent years have seen a push towards the development of acclimation protocols for imaging mice without anesthesia, but the results have been mixed. In parallel, imaging mice without anesthesia has become routine for complementary neuroimaging methods including wide-field fluorescence calcium (WF-Ca^{2+}) imaging. We present the first longitudinal protocol for simultaneous WF-Ca^{2+} and fMRI in awake mice. Our approach is comprised of a two-phase (biphasic) acclimation protocol that results in high-quality multimodal data, enabling direct comparison of neuronal mesoscopic and hemodynamic signals across brain states and time. Data from awake mice are compared with data from isoflurane-anesthetized imaging sessions to unlock state-dependent differences in functional connectivity, which show both convergent and divergent patterns between imaging modalities. Together, these results establish a framework for longitudinal awake multimodal imaging and uncover new insights into the neural and vascular functional organization of the mouse brain across states and time.

1. Introduction

Functional magnetic resonance imaging (fMRI) is a noninvasive tool for mapping large-scale brain networks that can be applied in both humans and animal models. These attributes make this modality a keystone technology within basic and translational neuroscience research[1-7]. Yet, the blood-oxygen-level-dependent (BOLD) fMRI signal is incompletely understood and offers low spatiotemporal resolution, relative to other imaging modalities[8]. In animal models, invasive methods can be applied in combination with fMRI to improve our collective understanding of brain function, and the BOLD signal[9]. Although rare, due to the challenges of combining imaging methods with fMRI, much stands to be gained through the development of strategic simultaneous multimodal imaging approaches[9,10].

Wide-field calcium (WF-Ca^{2+}) imaging provides a cell-type specific measure of concert neuronal activity at high spatiotemporal resolution, relative to fMRI[10-15]. Yet, the WF-Ca^{2+} imaging field-of-view (FOV) is limited to the cortex, whereas fMRI can access the whole-brain. These methods, when applied in combination, offer a unique opportunity to examine complementary measures of large-scale brain function[9]. The first simultaneous acquisition of WF-Ca^{2+} and fMRI data was described recently by our group[10,15], offering a unique framework to shed light into the neuro-vascular organization of the brain.

To-date, simultaneous WF-Ca^{2+} and fMRI has only been implemented in anesthetized mice. This is due to the significant challenges of performing BOLD-fMRI in awake animals. For a comprehensive discussion, see our recent systematic review, "*Where do we stand on awake fMRI in mice?*"[16]. Among our suggestions for how a concerted effort can help establish standardized and validated approaches for acclimating mice to undergoing fMRI whilst awake, we called for more studies which explicitly compare data collected from awake and anesthetized animals given the surprisingly limited number of direct comparisons in the literature[17-20].

Unlike in fMRI research, over the last decade it has become common to collect WF-Ca^{2+} imaging data from awake and behaving animals, e.g., [11,12,21,22] (for a review, see [23]). Notably, much of what has motivated a shift away from using anesthesia, within both WF-Ca^{2+} and fMRI applications, is a growing appreciation of the pronounced influence of anesthesia on neurogliovascular coupling, as well as large-scale brain activity patterns – much of which comes from the human and rodent fMRI literature[16,24,25,26-29]. Imaging awake animals also allows for assessment of brain activity during spontaneous behaviors as well as a broad range of tasks to be investigated. It is also noteworthy that the vast majority of research on humans is conducted on awake subjects and that inter-species translation may be improved by eliminating anesthesia from animal studies[9,11,12,16,30].

Here, we introduce and evaluate an experimental framework for acclimating mice to undergoing longitudinal, simultaneous WF-Ca^{2+} and fMRI data collection whilst in the awake state. We elected a biphasic approach comprised of a naïve animal training in incremental steps, followed by 'refresher' training prior to subsequent imaging sessions. Resultant subject motion, data exclusion, temporal signal-to-noise ratio (tSNR), and multimodal connectome specificity [31] (a measure of 'biologically plausible' relative connectivity or inter-regional activity synchrony) are used to infer multimodal data quality when data are acquired from awake or anesthetized mice. Differences in functional connectivity between awake and anesthetized imaging sessions are quantified at the connectome, network, and brain region level alongside inter-modality convergence.

Taken together, our findings indicate that the biphasic acclimation protocol successfully prepares mice for undergoing simultaneous WF-Ca^{2+} and fMRI awake imaging. The multimodal data acquired from awake animals are high-quality, and reproducible. Our results unveil a range of differences in multimodal connectivity spanning from connectome, to a *priori* network, to regional level. These show substantial intermodal convergence, as well as some notable divergence. This unique dataset lays a solid foundation for future studies aimed at dissecting large-scale brain function in awake mice.

2. Methods

All procedures were approved by the Yale Institutional Animal Care and Use Committee (IACUC) and followed the National Institute of Health Guide for the Care and Use of Laboratory Animals. Both biological sexes were included. Mice were group housed in individually ventilated cages with access to food and water *ad libitum*. Animals were on a 12h light/dark cycle. Data from awake mice are compared with data from anesthetized animals. All data was acquired concurrently. MRI data from anesthetized mice has been previously published [32].

2.1 Surgical procedures for multimodal imaging

See **Fig. 1A** for an experiment timeline. Mice undergoing multimodal imaging (N=11) underwent two surgical procedures as described previously [32,33].

2.1.1 Transverse sinus injections of a viral vector for uniform whole-brain fluorophore expression

To elicit whole-brain Ca^{2+} indicator expression in pyramidal neurons, transverse sinus injections of AAV_9.Syn.GCaMP6s.WPRE.SV40 (Addgene plasmid #100843; http://n2t.net/addgene:100843; RRID:Addgene_100843) were administered at birth (P_{0-1}) [34], **Fig. 1B**.

Pups were anesthetized using ice for 2–3min then transferred to a cool metal plate. A light microscope was used to visualize the transverse sinuses throughout the procedure. Sterilized fine scissors (Fine Science Tools, CA, USA) were used to make two small incisions (~2mm) in the skin above each transverse sinus. A glass capillary tube (3.5’ #3-000-203-G/X, Drummond Scientific Co, PA, USA), pulled using a P-97 pipette puller (Sutter Instruments, CA, USA) was used for the injection. Pipettes were filled with mineral oil (M3516, Sigma-Aldrich, NY, USA) and attached to a Nanoject III (Drummond Scientific Co) and MP-285 micromanipulator (Sutter Instruments). Most of the mineral oil was ejected and replaced with vector solution. The pipette tip was lowered through the skull and into the lumen of the transverse sinus (300–400mm below the skull surface). With no delay, 2μL of vector solution was injected at a rate of 20nL/sec. The pipette was retracted after a 5sec delay, and the procedure repeated targeting the opposite hemisphere. Delivery was verified by the observed blanching of the sinus. With the two injections complete, the skin was sealed with VetBond, and the pup placed on a warming pad. The procedure typically lasts 10min. The total volume (titer of 1×10^{13}vg/mL) of vector solution injected per pup was 4μL.

To minimize rejection by the mother, the whole litter was removed from the home cage together and kept on a warming pad while each pup underwent the procedure in sequence. Once all pups were alert, they were returned to the home cage and gently rubbed with home-cage bedding to mask foreign odors. This procedure resulted in cortex-wide GCaMP transfection and expression by adulthood in 10/11 pups. No WF-Ca^{2+} imaging was performed in the 11th animal due to hydrocephalus being observed in the MRI data (**2.6**).

2.1.2. Skull-thinning and head-implant placement for optical access to the cortex and immobilization

At 3 months-of-age (m), animals were initially anesthetized with 5% isoflurane (70/30 medical air/O_2) and secured in a stereotaxic frame (KOPF) using ear bars and an incisor bar. Isoflurane was then reduced to 2%. Eye ointment was applied; meloxicam (1-5mg/kg body weight) administered subcutaneously, and bupivacaine (0.1%, 0.04ml/5mg) injected locally at the incision site. Fur was removed and the scalp washed 3 times with betadine followed by ethanol (70%). The skin and soft tissue overlying the desired field-of-view (FOV) was surgically removed and the skull cleaned and dried. Antibiotic powder (Neo-Predef) was applied to the incision site, and isoflurane reduced further to 1.5%. Skull-thinning of the frontal and parietal skull plates was performed with a hand-held drill (FST, tip diameters 1.4 and 0.7mm), **Fig. 1C**.

Superglue (Locite) was applied to the exposed skull, followed by transparent dental cement C&B Metabond (Parkell). A pre-cut (Neurotechnology Core, USA) all-glass head-plate was attached to the dental cement prior to solidification. Animals were allotted 3 weeks to recover before any imaging data were collected or acclimation procedures begun.

2.2 Data acquisition

The dataset is comprised of longitudinal simultaneously acquired WF-Ca^{2+} and fMRI data (N=11) collected using an apparatus and imaging protocol we have described previously [10,13-15] as well as cross-sectional unimodal (MRI-only) data (N=11) to offset animal attrition (**2.5**). Mice in the unimodal dataset underwent head-plate implantation but not viral vector transfection (**2.1**). Imaging parameters (for both modalities) do not vary across timepoints or between groups. Mouse body weight was monitored, during acclimation training for awake imaging, as a proxy for chronic stress [16], **Fig. S1**.

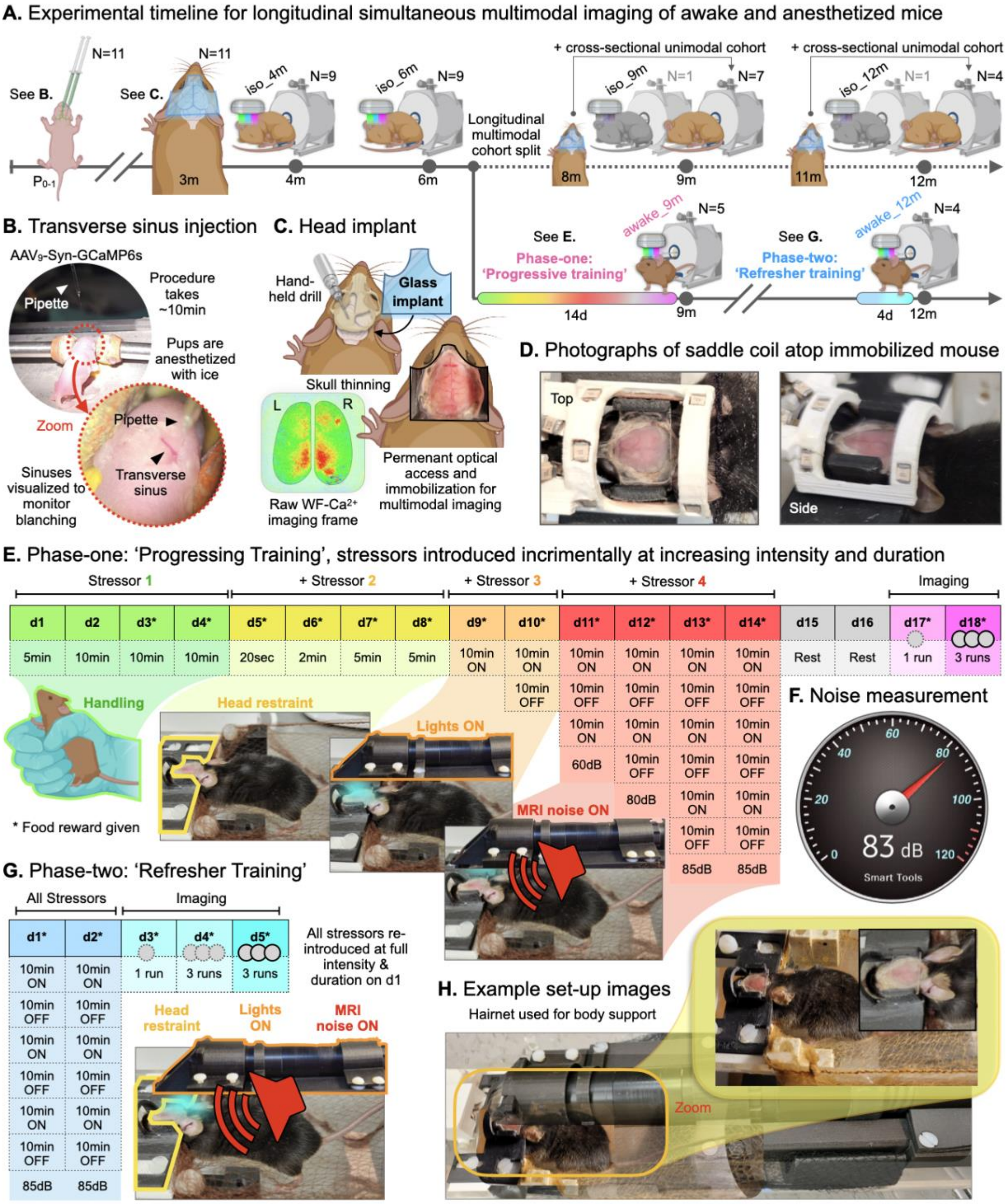

Stressor 1				+ Stressor 2				+ Stressor 3		+ Stressor 4						Imaging	
d1	d2	d3*	d4*	d5*	d6*	d7*	d8*	d9*	d10*	d11*	d12*	d13*	d14*	d15	d16	d17*	d18*
5min	10min	10min	10min	20sec	2min	5min	5min	10min ON	10min ON	10min ON	10min ON	10min ON	10min ON	Rest	Rest	1 run	3 runs
									10min OFF	10min OFF	10min OFF	10min OFF	10min OFF				
										10min ON	10min ON	10min ON	10min ON				
										60dB	10min OFF	10min OFF	10min OFF				
											80dB	10min ON	10min ON				
												10min OFF	10min OFF				
												85dB	85dB				

All Stressors		Imaging		
d1*	d2*	d3*	d4*	d5*
10min ON	10min ON	1 run	3 runs	3 runs
10min OFF	10min OFF			
10min ON	10min ON			
10min OFF	10min OFF			
10min ON	10min ON			
10min OFF	10min OFF			
85dB	85dB			

Fig. 1. Experiment overview. A. Mice in the longitudinal multimodal imaging group (N=11) underwent transverse sinus injections (**2.1.1**), head-implant placement (**2.1.2**), and two multimodal imaging sessions at 4 and 6m under anesthesia (isoflurane) (**2.2**). Mice were then randomly assigned to an awake and anesthetized group. Animals in the awake group underwent two phases of acclimation training for awake multimodal imaging (**2.3**) and were imaged after each phase at 9 and 12m. Two additional cross-sectional unimodal (MRI-only) groups were added at the 9 and 12m imaging timepoints (**2.5**). **B.** At birth, the viral vector AAV9.Syn.GCaMP6s.WPRE.SV40 is injected to induce whole-brain fluorescence as described previously [33]. **C.** At 3m, mice in the longitudinal multimodal imaging group underwent skull-thinning and head-implant placement. Mice in the unimodal (MRI-only) imaging groups also underwent head-implant placement one-month prior to imaging (**A.**). **D.** Photographs of the in-house built saddle coil for multimodal imaging. **E.** Protocol for acclimating mice to awake multimodal imaging (**2.3.1**). **F.** Protocol for re-acclimating mice to awake multimodal imaging (**2.3.2**). **G.** MRI-noise measurement example. Measured volumes were comparable between the real scanner and the mock set-up used for acclimation training (60-85dB). **H.** Additional photographs showing a mouse being prepared for awake multimodal imaging.

For mice that were imaged using anesthesia a free-breathing low-dose isoflurane regimen (~0.5-0.75%, in 50/50 medical air/O_2) was used as we have described previously [10,13,14]. Mice that were imaged whilst awake underwent a biphasic acclimation training protocol (**2.3**). This included both a 'Progressive Training' phase (**2.3.1**), conducted prior to the first awake imaging session, **Fig. 1E**, and a 'Refresher Training' phase (**2.3.2**), conducted prior to the second awake imaging session, **Fig. 1G**.

2.2.1 (f)MRI

Data were acquired on an 11.7T preclinical magnet (Bruker, Billerica, MA), using ParaVision v6.0.1. Body temperature was monitored (Neoptix fiber), maintained with a circulating water bath (36.6-37°C), and recorded (Spike2, Cambridge Electronic Design Limited). For acquisitions where anesthesia was used, breathing rate was measured using a foam respiration pad (Starr Life Sciences Corp., USA). During data acquisition, imaging and physiological measures were synchronized and recorded (Master-8 A.M.P.I., Spike2 Cambridge Electronic Design Limited).

Structural MRI. For image registration [10,15]:

1) A multi-spin-multi-echo (MSME) image sharing the same FOV as the fMRI data. Acquired with a repetition time (TR) of 2500ms and echo time (TE) of 20ms, 28 slices, two averages, and resolution of $0.1 \times 0.1 \times 0.31 mm^3$ (10min and 40sec),
2) A whole-brain isotropic 3D image using a MSME sequence, with $0.2 \times 0.2 \times 0.2 mm^3$ resolution, TR/TE of 5500/20ms, 78 slices, and 2 averages (11min and 44sec), and
3) A fast-low-angle-shot (FLASH) time-of-flight (TOF) angiogram (FOV, $2.0 \times 1.0 \times 2.5 cm^3$, covering the cortex), TR/TE of 130/4ms, and resolution of $0.05 \times 0.05 \times 0.05 mm^3$ (18min).

Functional MRI. Data were acquired using a gradient-echo echo-planar imaging (GE-EPI) sequence: TR/TE of 1.8sec/11ms, 334 volumes, 25 slices, and resolution of $0.31 \times 0.31 \times 0.31 mm^3$ resulting in near whole-brain coverage (~10min per run). For anesthetized imaging sessions, three runs were acquired per session (30min per mouse per timepoint).

Following the 'Progressive Training' for awake imaging (**2.3.1**), two consecutive days of imaging were performed. On day-one, mice underwent a truncated protocol that included only one functional imaging run (10min). On day-two, three functional imaging runs were acquired akin to the anesthetized imaging protocol (30min), **Fig. 1E**. Following 'Refresher Training' (**2.3.2**), three consecutive days of imaging were performed which included one, three, and three functional imaging runs (10, 30, and 30min), **Fig. 1G**.

2.2.2. WF-Ca^{2+} imaging

Data were acquired simultaneously with fMRI. The custom-built optical components which enable in-scanner WF-Ca^{2+} imaging were described by us previously [10,13,14]. Our in-scanner WF-Ca^{2+} imaging set-up has a FOV of 1.4cm^2 and collects optical images with a 25x25μm^2 resolution. Data were recorded using CamWare version 3.17. As we have described previously [10,13,14], data were acquired using two wavelengths: violet (395/25, GCaMP-insensitive) and cyan (470/24, GCaMP-sensitive) interleaved (LLE 7Ch Controller, Lumencor) at 20Hz, to enable frame-by-frame background correction, and a resultant effective sampling rate of 10Hz. Both wavelengths have an exposure time of 40ms and are separated by 10ms of no illumination to avoid rolling shutter artifacts.

2.3 Biphasic training for awake multimodal imaging

2.3.1 Phase-one: 'Progressive Training'

Performed prior to the first awake multimodal imaging session. Four sources of stress (stressors) were introduced incrementally at increasing intensity and duration during a 14-day period, **Fig. 1E**. Maximum duration (60min) and intensity were reached on day-13 (and repeated on day-14).

Stressors:

1) Experimenter handling (performed exclusively on day-1 through -4),
2) Head immobilization (with supported body suspension, i.e., hammock),
3) Illumination (necessary for WF-Ca^{2+} imaging), and
4) MRI-noise (a recording of the scanner).

After 4-days of exclusive handling by a single (female) experimenter, mice were exposed to the remaining stressors over a 10-day period. This was done within a mock-scanner environment comprised of a semi-circular tray which held the animal, a head-plate fixation apparatus, the MR-coil, and the optical imaging equipment, as well as a black tube which slid overtop of the whole set-up to mimic the scanner bore. The tray, and associated parts, were the actual components used during subsequent imaging sessions. A food reward (condensed milk) was provided from day-3 onwards.

From the conclusion of handling (i.e., beginning of head immobilization on day-5), the mouse's body was suspended in a 'hammock-like' bed constructed from a hairnet, **Fig. 1H**. This design grants body support without providing a surface for the mouse to effectively push against and likely helped preserve the integrity of the head-plate. One instance of head-plate detachment was observed (**2.5**).

For MR-noise, we used an application (Android 'Sound Meter', **Fig. 1F**) to measure true scanner noise (85–90dB). During training, the same application was used to monitor simulated scanning in the mock-scanner environment (60–85dB). Simulated scanning included a recording played back on speakers (Abramtek, China) placed next to the mock-scanner.

After 14-days of acclimation training, mice were given two days of rest (day-15 and -16), followed by two multimodal imaging sessions on consecutive days (day-17 and -18). On day-17, a truncated imaging protocol which included one functional run was performed (total scan time: 40min). On day-18, the full imaging protocol which included three functional runs was performed (total scan time: 60min). All anatomical imaging data needed for multimodal data registration (**2.4.3**) was collected at both imaging sessions.

2.3.2 Phase-two: 'Refresher Training'

For animals that have previously undergone Phase-one: 'Progressive Training' (**2.3.1**) and are not naïve to awake multimodal imaging. The protocol consisted of 2 days in the mock-scanner with all stressors reintroduced at full intensity and duration (60min), followed immediately by three multimodal imaging sessions on consecutive days, **Fig. 1G**. As done on the first imaging day following Phase-one, during the first imaging day following Phase-two (day-3), mice underwent a truncated imaging protocol which included one functional run (total scan time: 40min). The full imaging protocol, which included three functional runs (total scan time: 60min), was performed on the subsequent imaging days (day-4 and -5). All anatomical imaging data needed for multimodal data registration was collected at all imaging sessions (**2.4.3**).

Analyses were performed using data collected from awake mice on the last imaging day following Phase-one and Phase-two acclimation training. Specifically, data collected on day-18, following Phase-one, and day-5 following Phase-two.

2.4 Data preprocessing

2.4.1 fMRI

Data preprocessing was performed as described previously [32], using RABIES (Rodent automated BOLD improvement of EPI sequences) v0.5.0 [35]. All EPI data from each mouse (at each imaging session) was averaged to create a mean image, corrected for intensity inhomogeneities, and non-linearly registered to the corresponding isotropic MSME anatomical image. This reduces susceptibility-induced distortions. Slice time correction was applied to the native space timeseries.

To move the EPI data to common space, four transformations were applied: (1) motion correction, (2) mean fMRI → MSME, (3) MSME → within-dataset template, and (4) within-dataset template → out-of-sample template. We use an in-house out-of-sample template generated from N=162 datasets as described previously [32] which has been publicly shared (**2.4.3**). Transformations were concatenated then applied to each imaging frame. Data were resampled from the acquisition (0.31x0.31x0.31 mm^3 isotropic) to the template (0.2x0.2x0.2mm^3 isotropic) resolution. Results were visually inspected using the RABIES-QC (quality control) report. Motion parameters, as well as the global signal, CSF (cerebral spinal fluid), and white matter (WM) signals were regressed, and framewise displacement (FD) computed. Frames with FD>0.075mm were scrubbed and interpolation used to bridge any gaps [35]. Data were smoothed using a 0.4mm Gaussian kernel.

2.4.2 WF-Ca^{2+} imaging

Data were preprocessed as we have described previously [15]. Briefly, GCaMP-sensitive and -insensitive channels were smoothed with a 0.1mm sigma, and down-sampled by a factor of two in each spatial dimension. The GCaMP-insensitive channel was regressed from the GCaMP-sensitive channel and $\Delta F/F_0$ (F = fluorescence) computed for each run.

2.4.3 Multimodal data registration

Data from both imaging modalities were filtered (0.008-0.2Hz) and thirty seconds discarded from the beginning and end of each run. This mitigates edge artifacts caused by temporal filtering in the fMRI data [35] and eliminates the "photobleaching" artifact in the WF-Ca^{2+} imaging data [14]. Timepoints censored based on MRI-measured FD were also removed from the WF-Ca^{2+} imaging timeseries. Thus, the data from both modalities were temporally matched.

To spatially register the multimodal data, the WF-Ca^{2+} images were moved to the out-of-sample template using three transformations: two linear (1) WF-Ca^{2+} → Angiogram, and (2) Angiogram → MSME and one nonlinear (3) MSME → in-house template, as described by us previously [10,13,15]. This procedure utilizes specialized tools developed for this purpose within BioImage Suite, BIS (https://bioimagesuiteweb.github.io/webapp/), see **Fig. 2** in [15]. Via the BIS platform, the tools, atlases (**2.6.3**), and in-house out-of-sample template have been made freely available.

2.5 Exclusion criteria

N=11 pups underwent transverse sinus injections to elicit fluorophore expression (**2.1.1**). None were rejected by mothers or excluded based on an absence of sinus blanching (necessary for good transfection) [33]. Of these, N=2 were excluded due to hydrocephalus at 4m. Between the 6 and 9m imaging timepoints, N=2 mice died due to complications with housing. Before the 9m imaging timepoint N=1 was euthanized due to an eye infection that did not result from the head-plate. Remaining mice were randomly allocated to an awake (N=5), and anesthetized (N=1) multimodal imaging group. Between the 9 and 12m imaging timepoints, N=1 was excluded from the awake group due to poor head-plate integrity.

To augment the number of mice in the anesthetized group at the 9 and 12m imaging timepoints, MRI data was collected from two additional cohorts: N=7 at 9m, and N=4 at 12m (total N=11). As these mice did not undergo viral vector transfection to elicit fluorophore expression, no WF-Ca^{2+} imaging data were acquired from these animals. All mice underwent head-plate implantation for immobilization (**2.1.2**). Given the lack of WF-Ca^{2+} imaging data collected from anesthetized mice at the 9 and 12m imaging timepoints, these data were excluded from all analyses. From awake mice, only the n=3 runs acquired on the final day following each phase of training were analyzed (**2.3**).

Cohort:

1) 4m, N=9 (n=27 runs) anesthetized multimodal datasets,
2) 6m, N=9 (n=27) anesthetized multimodal datasets,
3) 9m, N=5 (n=15) awake multimodal, and N=7 (n=21) MRI-only anesthetized datasets,
4) 12m, N=4 (n=12) awake multimodal, and N=4 (n=12) MRI-only anesthetized datasets,

No mice were excluded during Phase-one: ‘Progressive Training’ (**2.3.1**) or Phase-two: ‘Refresher Training’ (**2.3.2**) due to weight loss, **Fig. S1**. At 6m, data from one mouse was excluded due to fMRI imaging artifacts. At 9m, data from one mouse in the MRI-only anesthetized group was excluded based on image registration failure. At the 4 and 6m imaging timepoints, no runs were excluded due to motion (>⅔ imaging frames >0.075mm FD) or the RABIES $DVARS_Z$ (derivative of timecourses' variance) criterion ($|DVARS_Z|>2.5$, [35]) which identifies imaging frames containing artifacts caused by motion as well as other sources. At the 9m imaging timepoint, 5 runs from awake mice were excluded due to FD or $DVARS_Z$. These came from two mice, thus all the data from one mouse was excluded. In addition, one run was excluded from a third mouse due to WF-Ca^{2+} imaging artifacts. At the 12m imaging timepoint, no datasets or runs were excluded.

Additional dataset information is summarized in **Table S1**.

Final dataset used:

1) 4m, N=9 (n=27 runs) anesthetized multimodal datasets,
2) 6m, N=8 (n=24) anesthetized multimodal datasets,
3) 9m, N=4 (n=9) awake multimodal, and N=6 (n=18) MRI-only anesthetized datasets,
4) 12m, N=4 (n=12) awake multimodal, and N=4 (n=12) MRI-only anesthetized datasets,

For the multimodal datasets, if data was excluded due to criteria applied to one modality (e.g., motion measured in the fMRI timeseries, or imaging artifacts in one or the other modality) the corresponding data in the second modality was also excluded. Thus, all the multimodal data are paired.

2.6 Data quality metrics

2.6.1 Temporal SNR

Functional MRI temporal signal-to-noise ratio (tSNR) was computed using RABIES [35] and [1] where μ_t is the mean signal intensity (SI) of a voxel over the course of a run and σ_t is the standard deviation (SD) of the voxel's SI over the same period. Similarly, the WF-Ca^{2+} imaging tSNR was computed using [1] in MATLAB (v2021b) where μ_t is the mean SI of a pixel within the frame range 1,000-1,500 (50sec extracted from the middle of each run).

$$tSNR_{voxel/pixel} = \frac{\mu_t}{\sigma_t} \qquad [1]$$

2.6.2 Motion

Motion in the fMRI data was estimated using RABIES while BIS was used to estimate motion in the WF-Ca^{2+} imaging data. When the 6 motion parameters, available from fMRI/RABIES, were considered independently it became clear that the vast majority of subject motion was in the up/down or dorsal/ventral direction, **Fig. S2A**. Given that WF-Ca^{2+} imaging offers a 2D view from above, it follows that these data were "blind" to these movements, **Fig. S2B**. Still, data excluded based on motion in the fMRI timeseries were also excluded from the WF-Ca^{2+} imaging dataset (**2.5**).

2.7 Functional connectivity

2.7.1 Brain atlases

Brain regions or nodes were based on the Allen Institute Common Coordinate Framework Reference Atlas (CCFv3) [36] as described by us previously[15]. Results were generated using a 3D (whole-brain, fMRI), 166-node, or 2D (cortical, multimodal), 46-node, bilaterally symmetric version of the atlas. Brain regions included in the 2D version were based on coverage in the WF-Ca^{2+} imaging FOV, **Fig. S3**;

brain regions included in the 3D whole-brain version were based on EPI slice package coverage, **Fig. S3**.

2.7.2 Connectomes and network definitions

To compute connectomes, WF-Ca^{2+} or fMRI signals within each region were averaged, and the inter-regional Pearson's correlation computed, and Fisher transformed. Connectomes were computed for each run using data residing in the in-house template space, as described by us previously [15,32].

Regions were subdivided into seven whole-brain networks [4,18,32], two of which were well represented within the cortex, **Fig. S3**. To provide a more fine-grained analysis of cortical network organization, these were further subdivided into four sub-networks.

2.7.3 Multimodal "specific connectivity"

Motivated by recent work which uses relative connectivity strengths to gauge 'biologically plausible' connectivity patterns [31], connectivity between the right and left primary somatosensory cortices (SSp), $SSp_R \leftrightarrow SSp_L$, were plotted against connectivity between SSp_R and the right anterior cingulate area (ACA), $SSp_R \leftrightarrow ACA_R$. In this framework, data with high connectivity strength ($R>0.1$) in $SSp_R \leftrightarrow SSp_L$ and coincident low connectivity strength ($R<0.1$) in $SSp_R \leftrightarrow ACA_R$ are considered desirable. These data were plotted alongside a reference distribution created from randomly chosen homotopic node pairs, and inter-hemispheric node pairs with n=1000 iteration for each.

2.8 Statistics

Significance is indicated as follows: *$p<0.05$, **$p<0.01$, ***$p<0.001$.

2.8.1 Multimodal signal quality-control

Unless stated otherwise, for all analyses assessing motion and tSNR, Kruskal-Wallis tests (MATLAB) were applied to test for differences across sessions. For any significant effects ($p<0.05$), post hoc pairwise multiple comparisons were performed and Bonferroni correction applied. Equality of variance was tested with Levene's test.

2.8.2 Connectome specificity

Session-specific shuffled distributions were generated as described in **2.7.3**. Distributions were compared using a two-sample Kolmogorov-Smirnov (KS) test, with Bonferroni correction applied to account for multiple comparisons. Further, the proportion of runs exceeding or falling below a 0.1 correlation threshold was computed to quantify the frequency of ‘specific’ connectivity across modalities.

2.8.3 Connectivity differences

<u>Edge-wise changes across states</u>. Pairwise functional connectivity values between cortical ROIs (main figures) or whole-brain ROIs (**Supplementary Material**) were compared across states (anesthetized vs. awake) using two-sample t-tests (*ttest2*, MATLAB) for each edge, followed by Benjamini-Hochberg correction to control for multiple comparisons; t-values are displayed without a threshold (bottom left half) and with a threshold for statistical significance applied (top right half).

<u>Cross-network analyses</u>. For both fMRI and WF-Ca^{2+}, the difference in functional connectivity between the baseline (iso_4m, anesthetized) and both the awake timepoints (awake_9m or awake_12m) was computed (ΔConnectivity) and a t-test (*ttest2*, MATLAB) was applied to test for differences of ΔConnectivity across modalities (Benjamini-Hochberg).

<u>Within network analyses</u>*.* Changes in functional connectivity were assessed between the anesthetized baseline timepoint (iso_4m) and each awake timepoint, independently (awake_9m or awake_12m), using a three-way ANOVA (factors: state (awake/anesthetized), hemisphere (intra/inter), and network), with Benjamini-Hochberg correction and non-parametric permutation tests (1,000 iterations) to evaluate shuffled-labels distributions.

<u>Cross-modal correlation analyses</u>*.* Two-sample t-tests to compare intra- versus inter-network correlations and one-sample t-tests against zero to identify significant coupling within each session were applied, with Bonferroni correction.

3. Results

3.1 Longitudinal multimodal imaging of awake mice does not cause weight loss

Animal weight, measured daily during acclimation and imaging, was used as a proxy for chronic stress [16]. Body weight was unaffected during both training phases and following awake imaging sessions, **Fig. S1**. No differences were found between mice that were imaged whilst awake and under anesthesia ($p>0.05$).

3.2 Multimodal signal quality

Data quality metrics, fraction of data excluded, motion, and tSNR, were compared between groups (awake versus anesthetized) and across time.

3.2.1 Awake mice moved more than anesthetized mice, but less after Phase-two: 'Refresher Training'

The fraction of imaging frames excluded from anesthetized animals was low, stable across time, **Fig. 2A**, and in-line with previous work [16,37], **Fig. S4A**. As expected, a greater fraction of imaging frames was excluded in the awake group, based on motion and $|DVARS_Z|$, relative to anesthetized animals at both the 9 and 12m imaging timepoints [16]. Overall, there was a significant session effect on fraction of frames excluded based on FD and on $|DVARS_Z|$ (Kruskal-Wallis, $p<0.001$ for both), whereby both awake sessions resulted in a significantly higher number of frames excluded, compared to anesthetized sessions (e.g. for 9m awake vs 4m anesthetized, $p<0.001$, corrected). Yet, between the first and second awake imaging sessions, the amount of motion was reduced (area under the curve 12m awake vs. 9m awake, $p<0.01$, corrected), **Fig. 2B&C**. In general, motion in the data acquired from both awake and anesthetized mice at all timepoints was in-line with previous work [16], **Fig. S4**.

3.2.2 Multimodal tSNR showed divergent patterns across modalities and dependence on whether data were acquired from awake or anesthetized mice

The WF-Ca^{2+} data showed a significant increase in tSNR across sessions, **Fig. 2D**, with higher signal stability observed in later imaging sessions (χ^2, $p<0.001$). Specifically, WF-Ca^{2+}-tSNR in a representative example cortical region (primary somatosensory, upper limb - SSp-ul) was significantly lower in 4m anesthetized mice compared to 9m awake ($p<0.01$, corrected) and to 12m awake ($p<0.001$, corrected), and also lower in 6m anesthetized compared to 12m awake ($p<0.01$, corrected). Conversely, the fMRI data showed the expected tSNR dependence on brain region (lower values near ear canals and in WM), **Fig. S5**. In anesthetized mice, average fMRI-tSNR in the same example cortical region, SSp-ul **Fig. 2D**, and other brain regions **Fig. S5**, was consistent across time and in-line with previous work [37]. Mice imaged whilst awake showed lower fMRI-tSNR, relative to anesthetized mice, at both the 9 and 12m imaging timepoints (e.g., 12m awake vs. 12m anesthetized, $p<0.01$, corrected).

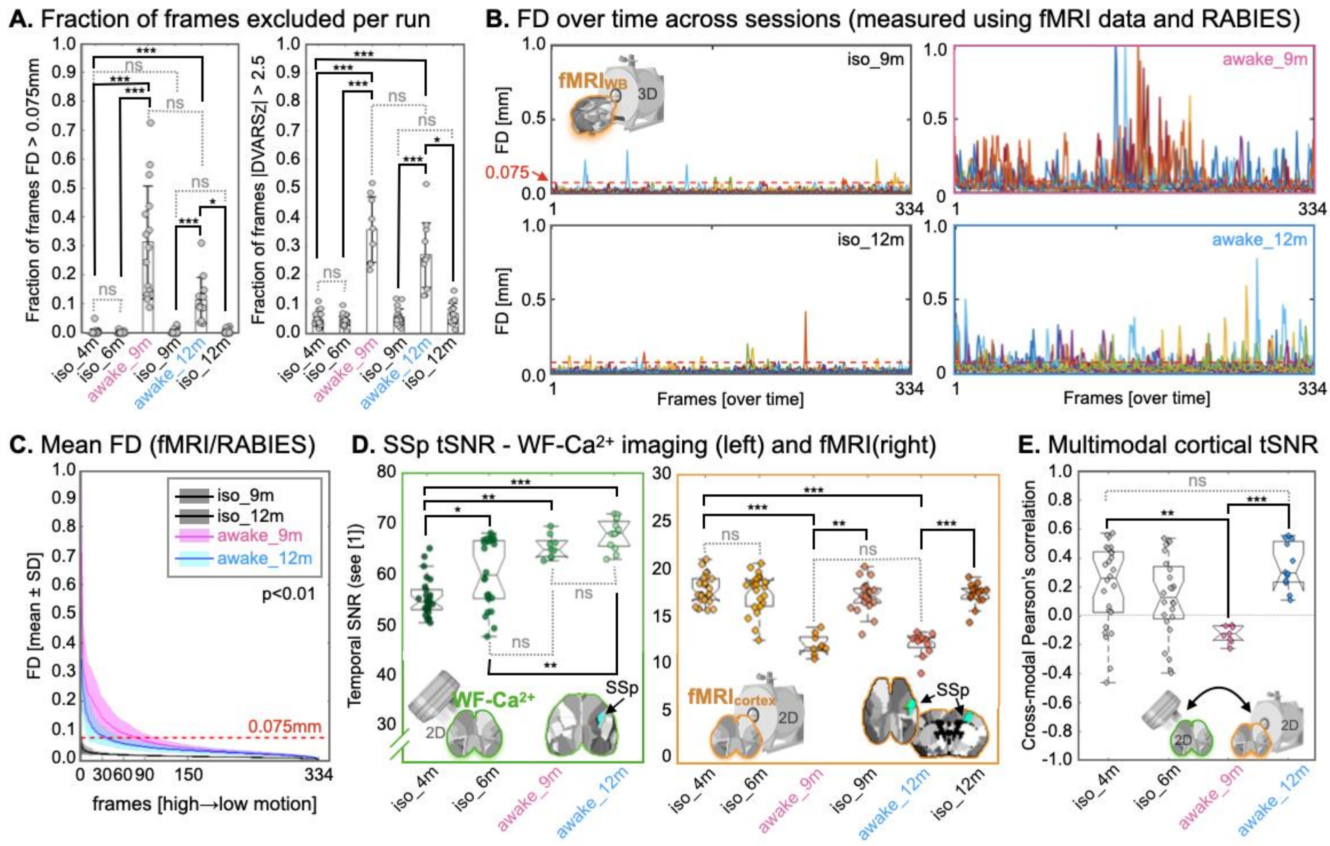

Fig. 2. Multimodal signal quality measures. A. Based on fMRI data, using RABIES, the fraction of imaging frames per run excluded based on motion FD>0.075mm (left), or $|DVARS_Z|>2.5$ (right). More imaging frames were excluded, based on either criterion, from awake relative to anesthetized imaging sessions. **B.** Also based on fMRI data, FD estimated by RABIES, over time. Different runs/mice are color-coded. The 0.075mm FD threshold for frame exclusion is indicated by a red dashed line. More motion was evident in awake relative to anesthetized imaging sessions. A reduction in motion was seen following the second, relative to the first, awake imaging session. **C.** FD (mean ± SD), measured using fMRI data and RABIES, sorted from highest to lowest. A significant cross-session effect was recovered (area under the curve tested with ANOVA and pairwise Bonferroni correction). **D.** Temporal SNR (tSNR) in a representative cortical region of interest (ROI), primary somatosensory, upper limb (SSp_R), computed for each run – after exclusion criteria were applied (**2.5**) – using WF-Ca^{2+} imaging (green, left) or fMRI (orange, right) data. Diverging patterns between imaging modalities were observed. **E.** Inter-modality tSNR correlation across all cortical ROIs (N=46). Corrected p-values are displayed: $*p<0.05$, $**p<0.01$, $***p<0.001$.

Importantly, while fMRI-tSNR variance was low and stable across all imaging sessions (p>0.05), WF-Ca^{2+} imaging data acquired from awake mice showed reduced tSNR variance relative to anesthetized animals (Levene's test, p<0.01), **Fig. 2D**. Finally, simultaneously acquired WF-Ca^{2+} and fMRI cortical tSNR were correlated (Pearson's R, MATLAB) across modalities, **Fig. 2E**. High variance in anesthetized relative to awake data was observed (p<0.01). Curiously, while no relationship between modalities was observed at 9m (median Pearson's R ± SD, -0.12 ± 0.06), a positive correlation was recovered at 12m (0.34 ± 0.16).

3.3 Multimodal "specific connectivity"

Connectivity between the right and left SSp (SSp-m), $SSp_R \leftrightarrow SSp_L$, were plotted against connectivity between SSp_R and ACA_R, $SSp_R \leftrightarrow ACA_R$, to gauge 'biologically plausible' connectivity patterns (**2.7.3**). This was motivated by previous work [31], which asserts—based on viral tracing experiments available from the Allen Institute, **Fig. 3A**—that coincident high connectivity strength (R>0.1) in $SSp_R \leftrightarrow SSp_L$ and low connectivity strength (R<0.1) in $SSp_R \leftrightarrow ACA_R$ should be recovered in 'high quality' data yielding 'specific functional connectivity'. To the best of our knowledge, this is the first application of this framework in WF-Ca^{2+} imaging data, **Fig. 3B**, and the first application in simultaneously acquired WF-Ca^{2+} and fMRI data.

3.3.1 Ample "specific connectivity" recovered in fMRI data acquired from anesthetized and awake mice

In the majority of runs (>85%), the fMRI data showed the anticipated pattern: high $SSp_L \leftrightarrow SSp_R$ and low, or absent, $SSp_R \leftrightarrow ACA_R$ connectivity, **Fig. 3C** (data points appearing in the quadrant outlined in yellow) indicating that, within this framework, these data would be considered 'high-quality', with 'specific' functional connectivity (FC). Relative to the reference distributions (**2.7.3**), anesthetized mice (grey) showed greater $SSp_L \leftrightarrow SSp_R$ connectivity than other homotopic node pairs (p<0.001, corrected), and lower, or absent, $SSp_R \leftrightarrow ACA_R$ connectivity relative to other intra-hemispheric node pairs (p<0.001, corrected), with one exception: $SSp_R \leftrightarrow ACA_R$ in iso_4m (p<0.05, corrected). Awake mice also showed greater SSp$_L$ ↔ SSp$_R$ connectivity than other homotopic node pairs ($p<0.01$ for awake_9m and $p<0.001$ for awake_12m, corrected), significant difference also between SSp$_R$ ↔ ACA$_R$ connectivity at 9m ($p<0.05$, corrected) but no significant difference between SSp$_R$ ↔ ACA$_R$ and other intra-hemispheric node pairs at 12m ($p>0.05$). This could indicate that, although SSp$_R$ ↔ SSp$_L$ connectivity strength may help to separate ‘high’ from ‘low’ quality datasets – at least more so than other inter-hemispheric node pairs – SSp$_R$ ↔ ACA$_R$ does not provide an equally useful second axis relative to other intra-hemispheric node pairs in data acquired from awake mice.

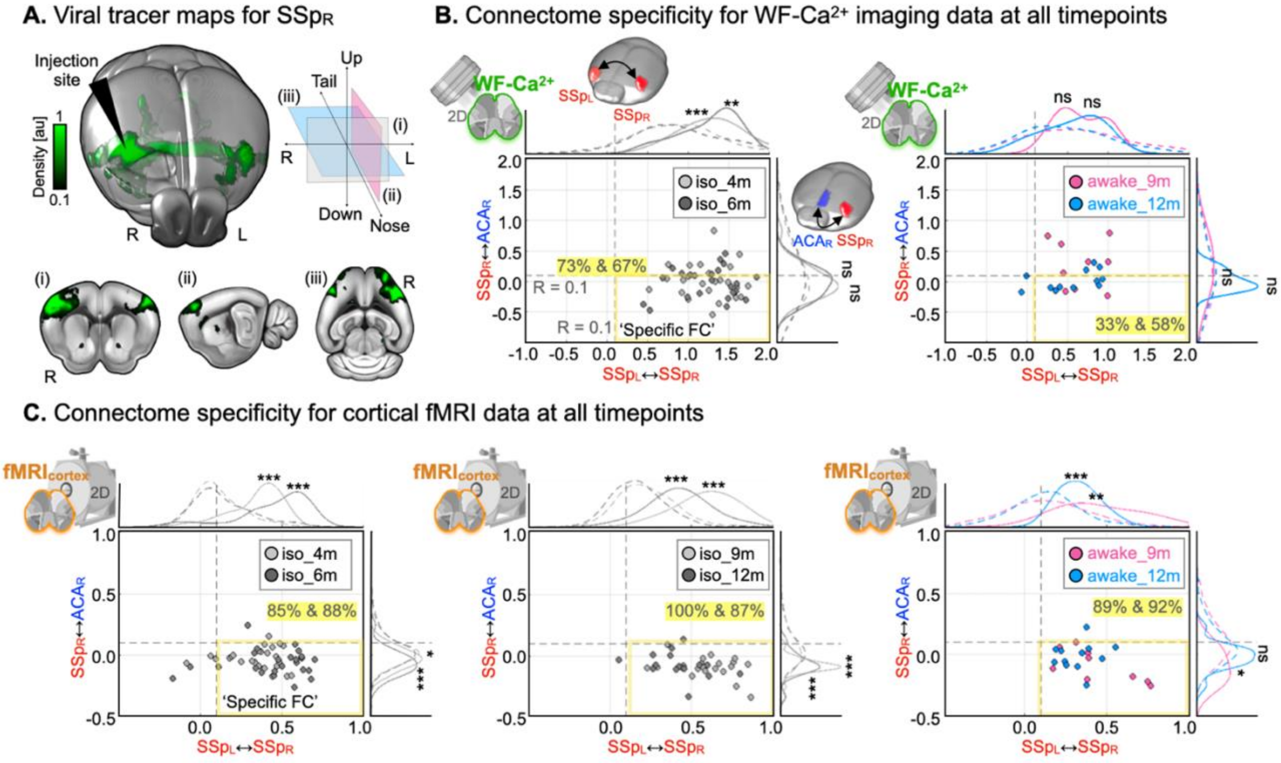

Fig. 3. Multimodal “specific connectivity”. A. Viral tracer map showing the physical connections of primary somatosensory area, mouth, SSp$_R$, based on viral vector injection (ID: 114290938, Allen Brain Connectivity Atlas) overlayed on an MRI template (average_template_50.nrrd, https://download.alleninstitute.org/informatics-archive/current-release/mouse_ccf/average_template/). The histology-based anatomical connection shown in this experiment motivates the “specific” functional connectivity (FC) framework for high versus low connectivity strengths SSp$_R$ ↔ ACA$_R$ and SSp$_R$ ↔ ACA$_R$, respectively. **B.** Scatterplots showing “specific FC” (**2.7.3**) using WF-Ca^{2+} imaging data. Data acquired from anesthetized mice are plotted in grey (left), while data acquired from awake mice are color coded (right). In the “specific connectivity” framework, high ($R>0.1$) SSp$_R$ ↔ ACA$_R$ (x-axis) versus low ($R<0.1$) SSp$_R$ ↔ ACA$_R$ (y-axis) connectivity strength should isolate ‘high-quality’ datasets in the lower right quadrant (highlighted in yellow). Above and to the right of the scatterplots, density distributions display kernel-smoothed observed (solid lines) and reference (dashed lines) distributions. Here, the reference distributions were generated from randomly selected intra- and inter-hemispheric node pairings. The fraction of runs identified as ‘high-quality’ are listed below the legend in each plot (highlighted in yellow). **C.** As in (**B.**) for fMRI data. Corrected p-values displayed: *$p<0.05$, **$p<0.01$, ***$p<0.001$.

3.3.2 "Specific connectivity" was less present in simultaneously acquired WF-Ca^{2+} imaging data

The same framework was applied to the simultaneously acquired WF-Ca^{2+} imaging data, **Fig. 3B**. In both anesthetized sessions (grey, 4m and 6m), there was a reproducible significant difference between $SSp_R \leftrightarrow SSp_L$ connectivity and random inter-hemispheric node pairs ($p<0.001$ and $p<0.01$, corrected, respectively). Yet, somewhat surprisingly, a lower fraction (<73%) of WF-Ca^{2+} imaging datasets, relative to fMRI datasets, were considered 'high-quality' due to variable $SSp_R \leftrightarrow ACA_R$ connectivity ($p>0.05$ for both anesthetized timepoints, 4 and 6m). Furthermore, WF-Ca^{2+} imaging datasets from awake mice (cyan and magenta)—which had higher tSNR than the anesthetized datasets (see **Fig. 2D**)—had the lowest fraction of 'high-quality'/'specific' data within this framework (<58%). Specifically, at neither awake timepoint, was $SSp_L \leftrightarrow SSp_R$ connectivity strength greater than other intra-hemispheric node pairings, or $SSp_R \leftrightarrow ACA_R$ connectivity strength less than other inter-hemispheric node pairings.

No runs were excluded from further analyses based on whether the anticipated connectivity pattern considered in this subsection was observed.

3.4 Connectivity differences between awake and anesthetized mice

Throughout this subsection, functional connectivity differences between data collected while mice were awake, at 9 and 12m, and data collected while mice were anesthetized, at 4 and 6m, were computed (t-test) and displayed as t-value maps (awake > anesthetized). Averaged connectomes are shown in **Fig. S3&S6**. Cortical regions, visible with both WF-Ca^{2+} and fMRI, **Fig. S3**, are considered for the majority of the analyses, and results for whole-brain analyses are shown in **Supplementary Material**. Results which use the 4m imaging timepoint, as the anesthetized baseline, are shown in **Fig. 4** for cortical regions and **Fig. S7** for whole-brain (fMRI only), more details below. When the 6m (anesthetized) imaging timepoint was used, in-place of 4m, very similar results were obtained, **Fig. S8**, more details below. Finally, also using only the fMRI data, a linear mixed model which considered whether mice were awake or anesthetized and mouse age, was generated, **Fig. S9**, more details later in this section.

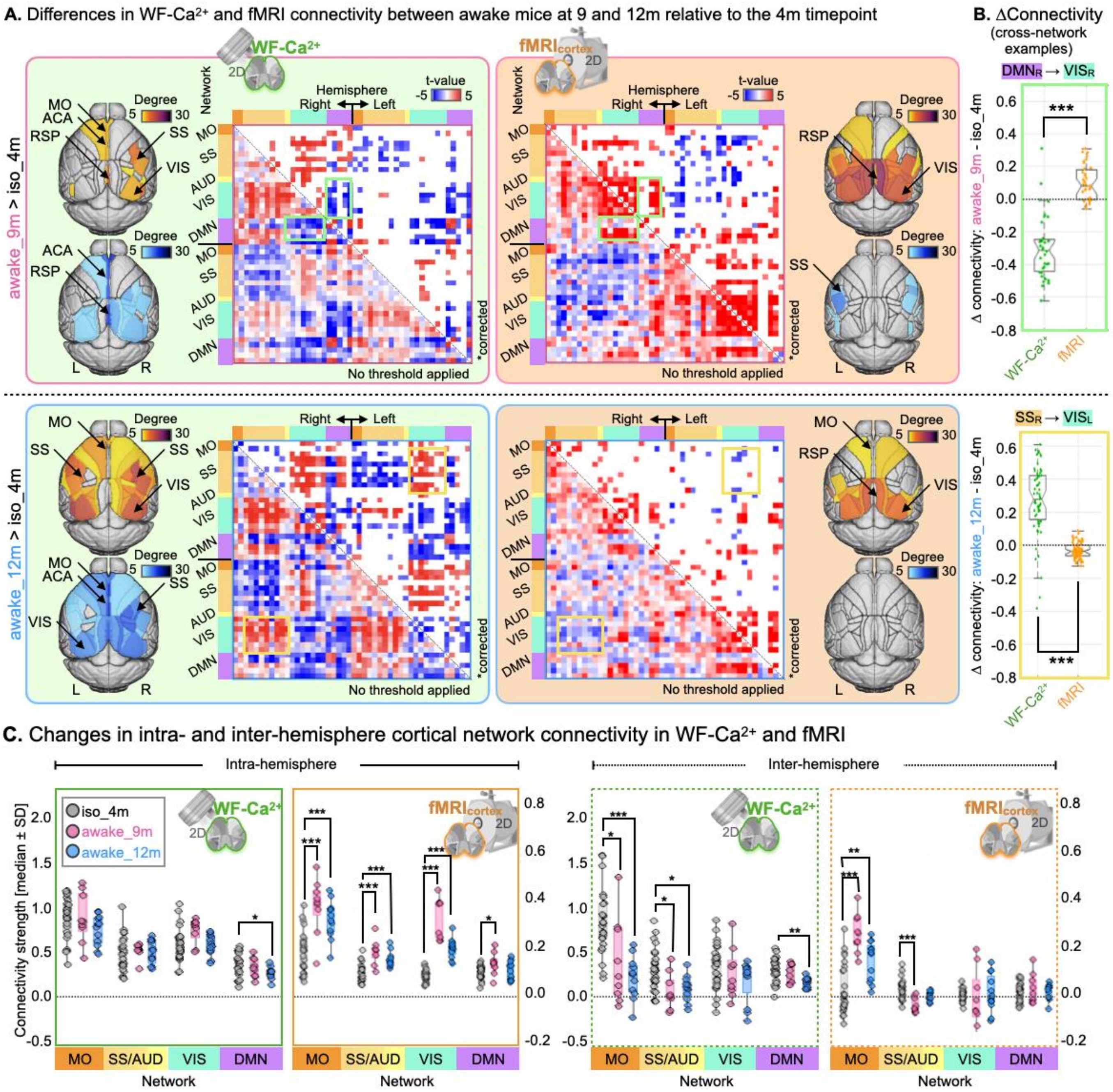

Fig. 4. Differences in cortical WF-Ca^{2+} and fMRI connectivity between anaesthetized and awake mice. A. Differences in WF-Ca^{2+} (left, green) and fMRI (right, orange) connectivity between the 9 (top, magenta outline) and 12m (bottom, cyan outline) awake imaging timepoints and the 4m (anesthetized) imaging timepoint. Results from a whole-brain analysis of the fMRI data are included in **Fig. S7**. An analysis which used the 6m (anesthetized) imaging timepoint, in-place of 4m, showed similar results, **Fig. S8**. Here, cortical regions, appearing in both imaging modalities **Fig. S3**, are shown. Matrices show significant connectivity differences (corrected, $p<0.05$) in the upper right half, and uncorrected differences in the bottom left half. Node-degree maps generated from corrected results appear to the right and left of each matrix (with a minimum of 5 edges as a threshold). Positive t-values (red, hot colors) indicate greater connectivity strength in awake mice. Negative t-values (blue, cool colors) indicate greater connectivity strength in anesthetized mice. **B.** Example of cross-networks connectivity differences between awake and anesthetized mice that were different between imaging modalities ($p<0.05$, corrected (Benjamini-Hochberg), *ttest2*, MATLAB). Networks are indicated in (**A.**) by color coded boxes. **C.** For *a priori* functional networks (**2.7.2**, **Fig. S3**), connectivity strength (median ± SD) intra- (left, solid border) and inter-hemisphere (right, dashed border) at each imaging timepoint. Corrected p-values: *$p<0.05$, **$p< 0.01$, ***$p<0.001$.

3.4.1 Widespread differences in cortical connectivity between awake and anesthetized mice were observed with both imaging modalities

At both the 9 and 12m awake imaging timepoints, relative to the 4m (anesthetized) imaging timepoint, WF-Ca^{2+} and fMRI showed widespread differences in cortical functional connectivity, **Fig. 4A**. Stronger connectivity was observed in awake relative to anesthetized mice in motor (MO), somatosensory (SS), retrosplenial (RSP), and visual (VIS) areas, with fMRI at 9m (orange top panel, magenta outline). At the same timepoint, weaker connectivity, in awake relative to anesthetized mice, was observed predominantly in inter-hemispheric somatosensory connections. At the 12m imaging timepoint (**Fig. 4A**, orange bottom panel, cyan outline), similar trends were recovered in the fMRI data, but the effects were noticeably diminished and less widespread. Conversely, the WF-Ca^{2+} imaging data showed an overall increase in connectivity differences that were more widespread at the 12 relative to the 9m imaging timepoint (**Fig. 4A**, green panels). These observations were all well replicated when the 6m (anesthetized) imaging timepoint was used in-place of the 4m imaging timepoint, **Fig. S8**. Of note, age-matched comparisons between awake and anesthesia (e.g. 9m awake vs. 9m anesthetized)—only possible in fMRI data (see **2.5**, and **Table S1**)—showed similar results to **Fig. 4A** for both awake timepoints (data not shown).

3.4.2 Brain regions showed convergent and divergent changes in connectivity across modalities and imaging timepoints in awake relative to anesthetized mice

Brain regions (or nodes) showing changes in connectivity in awake relative to anesthetized mice in both WF-Ca^{2+} (left) and/or fMRI (right) using data from the 9 (top) and/or 12m (bottom) imaging timepoints (i.e., imaging data following the initial progressive training, or the refresher training, respectively) were identified using the corrected matrices in **Fig. 4A** (upper right halves), and displayed as node-degree maps for both positive edges (awake > anesthetized) and negative edges (awake < anesthetized) (**Fig. 4A**, node-degree maps overlayed on brain templates, red and blue hues, respectively). Further, common edges, across imaging modalities and timepoints, were identified by taking the product of the binarized matrix pairs. Node-degree, and bilateral symmetry, were used to identify regions showing common or divergent differences in connectivity between awake and anesthetized mice, across imaging modalities and timepoints, **Table 1**.

Table 1. Nodes showing connectivity differences in awake vs. anesthetized mice in multimodal data

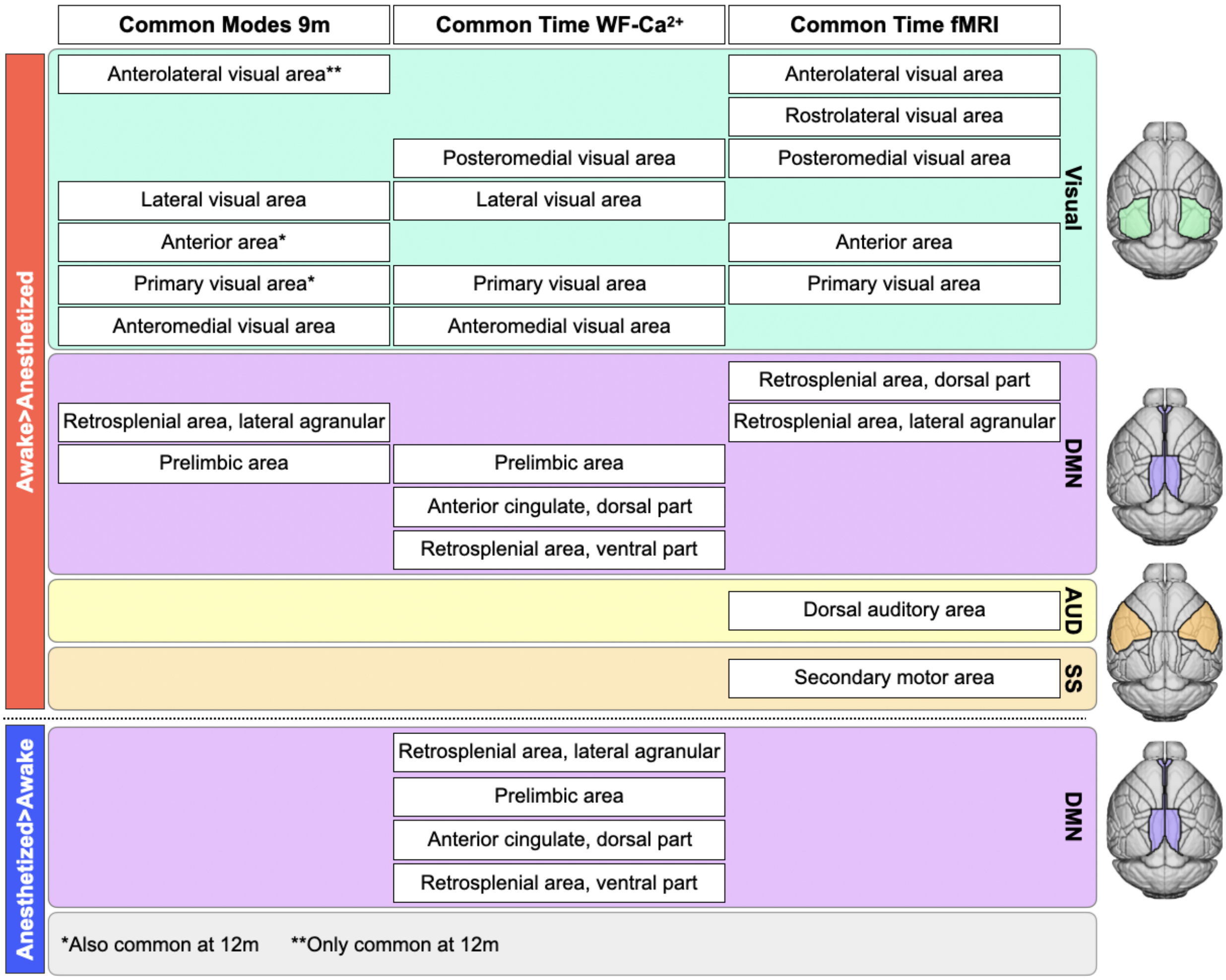

		Common Modes 9m	Common Time WF-Ca^{2+}	Common Time fMRI
Awake>Anesthetized	Visual	Anterolateral visual area**		Anterolateral visual area
				Rostrolateral visual area
			Posteromedial visual area	Posteromedial visual area
		Lateral visual area	Lateral visual area	
		Anterior area*		Anterior area
		Primary visual area*	Primary visual area	Primary visual area
		Anteromedial visual area	Anteromedial visual area	
	DMN			Retrosplenial area, dorsal part
		Retrosplenial area, lateral agranular		Retrosplenial area, lateral agranular
		Prelimbic area	Prelimbic area	
			Anterior cingulate, dorsal part	
			Retrosplenial area, ventral part	
	AUD			Dorsal auditory area
	SS			Secondary motor area
Anesthetized>Awake	DMN		Retrosplenial area, lateral agranular	
			Prelimbic area	
			Anterior cingulate, dorsal part	
			Retrosplenial area, ventral part	

*Also common at 12m **Only common at 12m

Nodes that showed greater connectivity in awake relative to anesthetized mice at 9m in both imaging modalities included visual areas and regions within the default mode network (DMN), **Table 1** (column 1). At the 12m imaging timepoint, a subset of visual areas showed the same pattern. In the WF-Ca^{2+} imaging data, greater connectivity in awake relative to anesthetized mice was recovered at both imaging timepoints in visual areas and regions within the DMN, **Table 1** (column 2). The opposite pattern, increased connectivity in anesthetized relative to awake mice, was also observed with WF-Ca^{2+} imaging within the DMN. In parallel, the fMRI data showed greater connectivity in awake relative to anesthetized mice at both timepoints in visual areas and regions within the DMN as well as in the dorsal auditory (AUD) area, and secondary motor area, **Table 1** (column 3).

Overall, there were several brain regions that showed consistent changes in connectivity between awake and anesthetized mice across modalities and imaging timepoints. These were dominated by increased connectivity in visual areas and regions within the DMN. However, there were also clear instances when the two imaging modalities showed different or diverging patterns. As above (**3.4.1**), these observations were well replicated when the 6m (anesthetized) imaging timepoint was used in-place of the 4m imaging timepoint.

3.4.3 A priori cortical brain networks showed differences in connectivity between awake and anesthetized mice that differed between imaging modalities

Brain regions were organized into networks, **Fig. S3**. In the previous subsection (**3.4.2**) brain regions showing differences in connectivity between awake and anesthetized mice were identified alongside the networks they belonged to (bottom-up). When *a priori* networks, or inter-network pairs, were considered (top-down), differences in connectivity between awake and anesthetized mice within or between networks revealed more divergent patterns between imaging modalities, **Fig. 4B&C**.

For WF-Ca^{2+}, the comparison of the anesthetized baseline (iso_4m) with the 9m awake session showed significant main effects for hemisphere (inter/intra) ($F_{1,267}=19.81$, $p<0.05$) and network ($F_{3,267}=7.15$, $p<0.05$), as well as significant interactions between state (awake/anesthetized) x hemisphere ($F_{1,267}=13.26$, $p<0.001$), state x network ($F_{3,267}=3.10$, $p<0.05$), and hemisphere x network ($F_{3,267}=4.13$, $p<0.01$). Similarly, the comparison of the anesthetized baseline with the 12m awake timepoint showed significant main effects of hemisphere ($F_{1,291}=24.13$, $p<0.05$) and significant interactions between state x hemisphere ($F_{1,291}=17.25$, $p<0.001$), state x network ($F_{3,291}=7.08$, $p<0.001$), and hemisphere x network ($F_{3,291}=4.40$, $p<0.01$). Overall, differences in *a priori* network connectivity between awake and anesthetized mice were more prominent inter-hemisphere than intra-hemisphere in the WF-Ca^{2+} imaging data, **Fig. 4C**. Motor, somatosensory and auditory networks showed decreases in inter-hemispheric connectivity at 9 and 12m awake timepoints, relative to 4m anesthetized (Motor: $p<0.05$/$p<0.001$, respectively; somatosensory/auditory: $p<0.05$ for both, pairwise post-hoc test, Benjamini-Hochberg, corrected). The default-mode network showed the same at 12m intra- as well as inter-hemisphere, whilst no other differences in intra-hemispheric network connectivity were observed with WF-Ca^{2+} imaging.

Dissimilarly, fMRI showed widespread increases in *a priori* network intra-hemispheric connectivity at 9 and 12m, relative to 4m, with the sole exception of the default-mode network at 12m. The comparison between the anesthetized baseline (iso_4m) with 9m awake, revealed a significant main effect of hemisphere ($F_{1,267}$=98.58, p<0.001) and significant interactions between state x hemisphere ($F_{1,267}$=28.15, p<0.001), state x network ($F_{3,267}$=25.53, p<0.001), and hemisphere x network ($F_{3,267}$=3.11, p<0.05). Very similar results were found for 12m awake compared to the 4m anesthesia baseline (significant main effect of hemisphere ($F_{1,291}$=50.67, p<0.01) and significant interactions between state x hemisphere ($F_{1,291}$=12.54, p<0.001), state x network ($F_{3,291}$=16.91, p<0.001), and hemisphere x network ($F_{3,291}$=7.9, p<0.001). Further, fMRI inter-hemispheric connectivity in *a priori* networks showed a divergent pattern, with motor areas being increased at 9 and 12m, while somatosensory/auditory decreased.

The robustness of these observations, for both WF-Ca^{2+} and fMRI, is supported by permutation tests where subject and state (awake or anesthetized) were randomly shuffled in a permutation test and compared to the true observed values (n=1000), across all networks, **Fig. S10A**.

3.4.4 Node and network analyses can lead to seemingly different conclusions

When brain regions (bottom-up) were considered (**3.4.2**), the nodes identified as playing a prominent role in distinguishing awake from anesthetized mice included visual areas as well as regions within the DMN, **Table 1**. Although some differences in the corresponding networks (visual and default-mode networks, **Fig. 4C**) were recovered (**3.4.3**) – intra/inter-hemispheric default-mode connectivity at 12m, in the WF-Ca^{2+} imaging data, and intra-hemispheric visual connectivity at 9 and 12m in the fMRI data – they were not among the more salient effects. This is a result of considering a network in its entirety, which can obscure contributions from individual nodes, opposing contributions from different nodes, or connections, within the same network (e.g., DMN, **Table 1**), and contributions from inter-network connectivity, **Fig. 4B**.

3.4.5 Whole-brain a priori networks observed with fMRI show widespread differences between awake and anesthetized mice that are independent of mouse age

Seven *a priori* networks which span the whole-brain were evaluated using the fMRI data, **Fig. S3**. As in the multimodal analyses of cortical connectivity, widespread differences in whole-brain connectivity between awake and anesthetized mice were observed at the 9 and 12m imaging timepoints relative to the 4m (anesthetized) imaging timepoint, **Fig. S7**. Similarly, an overall decrease in these differences was apparent in the data collected at 12 relative to 9m, **Fig. S7A**. When *a priori* network connectivity, both intra- and inter-hemisphere, was compared across imaging timepoints, **Fig. S7B**, both patterns of increased connectivity in awake relative to anesthetized mice and the opposite pattern were observed. For the 9m awake vs 4m anesthetized comparison, the ANOVA showed a significant main effect of hemisphere ($F_{1,468}$=58.44, p<0.001) and significant interactions between state x hemisphere ($F_{1, 468}$=85.89, p<0.001), state x network ($F_{6,468}$=13.85, p<0.001), and hemisphere x network ($F_{6, 468}$=9.61, p<0.001). Similarly, iso_4m vs. awake_12m showed a significant main effect of hemisphere ($F_{1,510}$=62.96, p<0.001), network ($F_{1,510}$=4.22, p<0.05) and significant interactions between state x hemisphere ($F_{1, 510}$=36.57, p<0.001), state x network ($F_{6, 510}$=12.6, p<0.001), and hemisphere x network ($F_{6, 510}$=9.44, p<0.001). Overall, intra-hemisphere, connectivity in awake relative to anesthetized mice increased, with the exception of within the default-mode network, which showed no effect, and the striatal network which showed increased connectivity in anesthetized relative to awake mice. Conversely, inter-hemispheric connectivity was more widely increased in anesthetized relative to awake mice. As above, the robustness of these observations was supported by permutation tests where subjects and state (awake or anesthetized) were randomly permuted, **Fig. S10B**. Furthermore, when the 6m (anesthetized) imaging timepoint was used, in-place of 4m, similar results were obtained.

The properties of the dataset (**2.5**) allowed for a linear mixed model to be generated which jointly accounted for differences in connectivity associated with animal state (awake or anesthetized) and age based on fMRI, but not WF-Ca^{2+} imaging, data. Two models were generated, one using data from the cortex, matching the WF-Ca^{2+} imaging FOV, and one using data from the whole-brain, **Fig.**

S9A&B respectively. Both showed that the effects of age on differences in connectivity were minimal compared to the effects of state (awake versus anesthetized).

3.5 Cross-modality correlation of WF-Ca^{2+} and fMRI connectivity

Diverging patterns in intra- and inter-hemispheric connectivity across cortical networks in WF-Ca^{2+} and fMRI data (**3.5.3**) motivated an examination of cross-modality connectivity agreement within and between networks, **Fig. 5A**, as well as intra- and inter-hemisphere, **Fig. 5B**. WF-Ca^{2+} and fMRI connectomes were separated into cortical networks within right and left hemispheres and vectorized. Due to its small size (two regions per hemisphere), the motor network was excluded. Cross-modality correlation (Pearson's R) was computed for each pair of networks (and hemispheres) at each imaging timepoint.

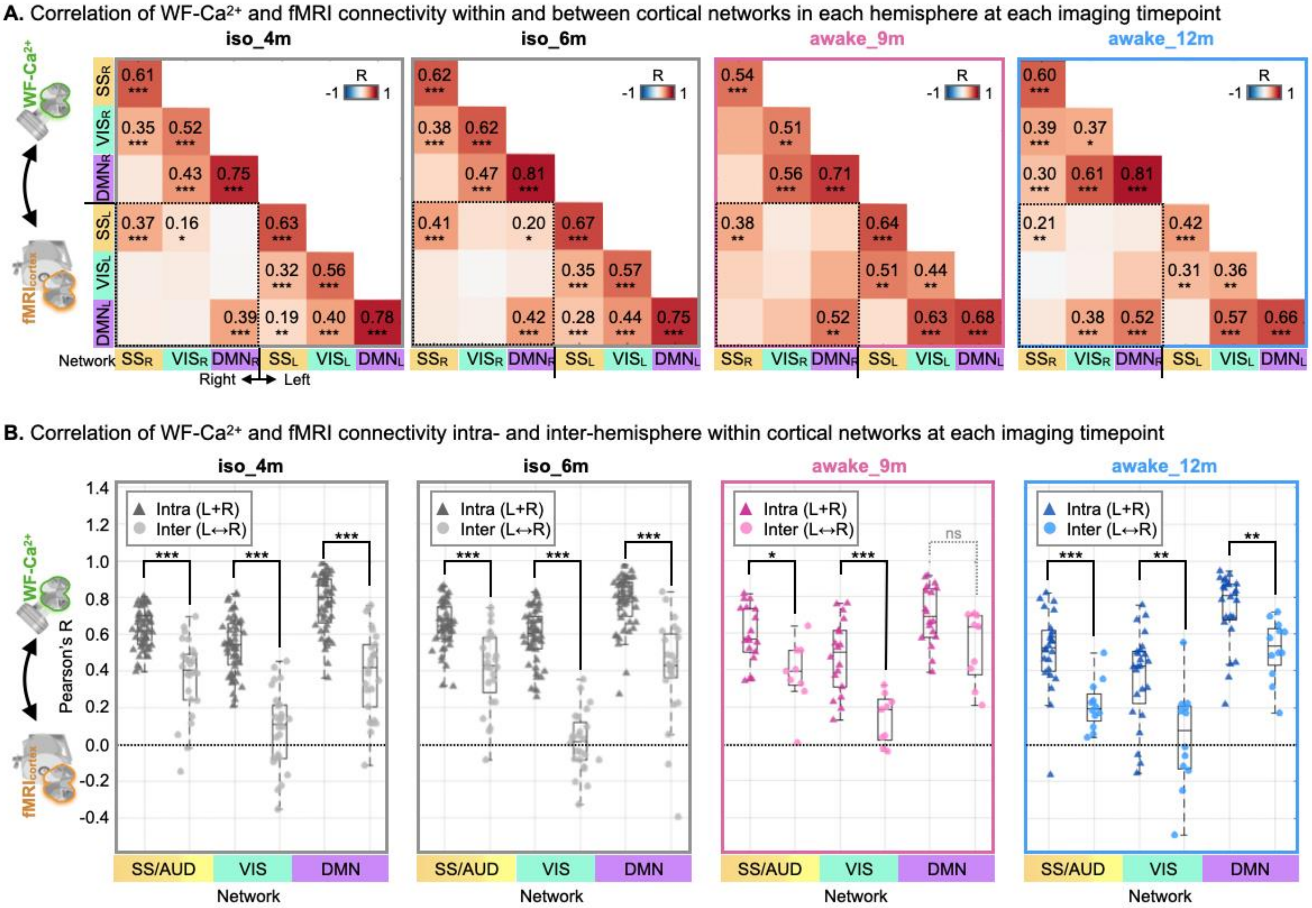

Fig. 5. Correlation of WF-Ca^{2+} and fMRI connectivity across cortical networks and imaging timepoints. A. At each imaging timepoint (4, 6, 9, and 12m), matrices showing the mean correlation of WF-Ca^{2+} and fMRI connectivity within and between cortical networks. Data from right and left hemispheres, as well as inter-hemisphere (black dotted lines), are shown. **B.** Scatterplots showing intra- and inter-hemisphere cross-modality correlation of WF-Ca^{2+} and fMRI connectivity within cortical networks (intra/inter are denoted by triangles/circles, respectively) at each imaging timepoint. Corrected p-values are displayed: *p<0.05, **p< 0.01, ***p<0.001.

3.5.1 Patterns in cross-modality connectivity were well-preserved across imaging timepoints and between awake and anesthetized imaging sessions

At both anesthetized, 4 and 6m, and awake, 9 and 12m, imaging timepoints, remarkably similar inter-modality connectivity patterns were observed. Within cortical networks, in both the right and left hemispheres, high inter-modality correlations were recovered – especially within the DMN, **Fig. 5A** (values along the diagonal). Across hemispheres, there was much less inter-modality agreement, **Fig. 5A** (dashed line box).

3.5.2 Across cortical networks, and imaging timepoints, correlation strength between WF-Ca^{2+} and fMRI connectivity was lower inter- versus intra-hemisphere

Using connectomes generated from each run (10mins), correlation strength between WF-Ca^{2+} and fMRI connectivity for each cortical network, intra- and inter-hemisphere are shown in **Fig. 5B**. Across cortical networks and imaging timepoints, intra-hemisphere connectivity across imaging modalities was more correlated than inter-hemisphere connectivity, with the sole exception of the DMN at the 9m. This pattern was reminiscent of observations made in our previous work, which considered node-connectivity across imaging modalities intra- and inter-hemisphere [10].

4. Discussion

This work establishes a biphasic acclimation protocol for longitudinal simultaneous WF-Ca^{2+} and fMRI data collection in awake adult mice. The experimental framework incorporates elements from a recent systematic review where we highlighted the importance of comparing data collected from awake and anesthetized animals alongside a critical evaluation of signal quality given the paucity of such investigations in the current literature[16]. Beyond the technical advancement needed for performing these experiments, this work provides a novel characterization of large-scale brain connectivity differences between awake and anesthetized mice using unique multimodal data. Coincident inter-modal convergent and divergent patterns in large-scale functional organization are revealed and considered within the context of previously observed differences in data collected from awake and anesthetized mice which used either WF-Ca^{2+} [38,39] or fMRI[17-20].

4.1 Multimodal data quality

4.1.1. Motion

Each element of the biphasic acclimation protocol was based on evidence gleaned through our systematic review[16]. This included the 14-day duration of Phase-one: ‘Initial Progressing Training’, gradual and incremental introduction of stressors, use of a food-reward, biphasic design, use and key elements of a mock scanner environment (e.g., recorded scanner noise), as well as use of the real system for acclimation purposes. These efforts contributed to achieving motion estimates (i.e., |FD|) which were comparable to previous high-quality work at both timepoints where mice were imaged whilst awake, **Fig. S4**. The decrease in subject motion which followed Phase-two: ‘Refresher Training’, a full two-months following the initial phase, **Fig. 2C**, could motivate an investigation into a more distributed, rather than intensive, acclimation protocol as part of future work. That the study design implemented here did not include a group which underwent Phase-one: ‘Initial Progressive Training’ prior to the 12m imaging timepoint precludes concluding that a biphasic protocol reduces subject motion based on the current study results alone.

Simultaneous WF-Ca^{2+} imaging showed minimal motion in the X–Z plane (the only estimate possible using these 2D data). This is in-line with the observation that the majority of motion in the fMRI data is along the Y-axis, which is “invisible” to WF-Ca^{2+} imaging, **Fig. S2**. Body-induced B_0 inhomogeneities are also likely contributors to perceived motion in the fMRI data that have no correlate in WF-Ca^{2+} imaging. A deeper phenotyping of how subject motion manifests in multimodal data and its impact on measures of brain function will be the focus of future work. Other avenues include the future use of a body restraint system[16,40,41] (as the mouse body was unrestricted in this study), magnetic field correction [42], or the implementation of novel MRI-acquisition strategies that are insensitive to body movement [43-45].

4.1.2. Temporal SNR

In the fMRI data, tSNR at all timepoints was comparable to estimates from anesthetized animals in a recent multi-centre study (see **Fig. 1** in [37]). Still, the tSNR in the fMRI data acquired from awake mice was lower than in data acquired from anesthetized mice. In the corresponding WF-Ca^{2+} imaging data, tSNR showed the opposite pattern, **Fig. 2D**. This is unsurprising given the distinct signal and noise sources, including head and body motion (**4.1.1**), which affect tSNR differentially in each modality [46-48]. The positive correlation between WF-Ca^{2+} and fMRI tSNR observed at the 12m imaging timepoint is intriguing, **Fig. 2E**. This observation, alongside the mismatch at the 9m awake imaging timepoint, may suggest that tSNR is dominated by common sources of signal and noise at 12m, but opposing or mismatched sources at the earlier, 9m, awake imaging timepoint (e.g., body motion).

4.1.3. Stress

Acclimation protocols for undergoing imaging whilst awake aim to reduce animal motion, improve tSNR, and reduce animal stress through exposure to the conditions of the experiment without any adverse events. Ideally, through acclimation, the animal learns that the procedures are not harmful, and this reduces stress. However, over-training has been posited as equally undesirable as it can result in a depressive phenotype due to prolonged, low-level, stress[49]. Striking the 'ideal' balance between these extremes–both of which have known effects on brain function [49-51]–is a challenging and currently unsolved problem. Stress, both acute and chronic, is difficult to measure in mice and has not been thoroughly characterized in the existing mouse fMRI literature[16]. Further, these concerns have been typically ignored in WF-Ca^{2+} imaging experiments due to the environment being considered much less stressful overall, with a few notable exceptions [52-54]. A thorough investigation of the effects and presence of acute and chronic stress was beyond scope of this investigation. However, animal body weight, measured daily during acclimation and imaging, was used as a proxy for long-term stress [55]. Every animal in this study maintained a stable weight throughout acclimation and imaging, with no differences between awake and anesthetized groups, **Fig. S1**. Future work will include more comprehensive measures of acute and chronic stress using behavioral monitoring, heart rate variability [56,57], and/or blood corticosterone measurements [16,18].

4.1.4. Specific connectivity

This metric was recently introduced by Grandjean and colleagues ([31,37]) for assessing mouse fMRI data quality. It is based on quantifying two “biologically plausible” measures of functional connectivity, one posited to show high connectivity ($SSp_R \leftrightarrow SSp_L$), and the second posited to show low, absent, or negative connectivity ($SSp_R \leftrightarrow ACA_R$), based on the physical/structural connectedness of these brain regions, **Fig. 3A**. A large fraction of the fMRI data collected from anesthetized mice in this study was categorized as “high-quality” based on this metric (85-100% depending on the imaging timepoint), **Fig. 3C**. Functional MRI data acquired from awake mice, encouragingly, showed similarly high rates (89 and 92%) despite lower tSNR. Notably, the specificity results across all fMRI data were aligned with previous literature (~80% in a recent multi-centre mouse fMRI study [37]). However, counterintuitively, extending this assessment to the simultaneously acquired WF-Ca^{2+} imaging data collected from anesthetized mice, uncovered middling rates of “high-quality” data (67 and 73%) driven by variability in $SSp_R \leftrightarrow ACA_R$ connectivity. Further, low rates (33 and 58%) were observed in WF-Ca^{2+} imaging data acquired from awake mice despite these having higher and less variable tSNR, **Fig. 2D**. Given that this metric is based on a viral tracer map, it should be more closely related to WF-Ca^{2+} imaging results, than those gleaned from fMRI data (despite this metric having been originally developed for assessing fMRI data quality). That the opposite pattern is uncovered calls into question using physical/structural connectedness to assess the quality of functional data. Overall, this weighs-in on a long-standing debate regarding the relatedness of brain structure and function in both human[58-60] and mouse [61-63] literature.

4.2 Functional connectivity

4.2.1. Functional MRI

Data from awake, relative to anesthetized mice, showed widespread increases in intra-hemispheric connectivity strength alongside decreases in inter-hemispheric connectivity strength within *a priori* cortical and whole-brain networks, **Fig. 4C**, **S7 & S9**. With a few noted exceptions (**3.4**). Similar patterns have been previously reported using both mice[57,64] and rats[65], and are purported to reflect enhanced network segregation and reduced global synchrony with wakefulness [17,18,20,56,66,67], see

Table 3 in [16]. Although these patterns were recovered at both the 9 and 12m imaging timepoints, the effects were stronger at the 9m imaging timepoint following Phase One: ‘Initial Progressive Training’. Using the fMRI data, it was inferred that the attenuation of these effects were not attributable to animal age, **Fig. S9**. It is possible that the completion of additional acclimation (i.e., Phase Two), was responsible, but this will need to be validated in a future study.

4.2.2. WF-Ca^{2+} imaging

Relative to observations made using fMRI data, simultaneously acquired WF-Ca^{2+} imaging showed more stable intra-hemisphere connectivity strength between awake and anesthetized mice within *a priori* cortical networks, while differences in inter-hemispheric connectivity strength showed a mixture of convergent (motor and visual) as well as divergent (motor and DMN) patterns, **Fig. 4C**. It was also apparent, that the WF-Ca^{2+} imaging data showed more widespread differences in connectivity strength between awake and anesthetized mice at the 12m imaging timepoint (whereas fMRI showed the opposite pattern), **Fig. 4A**.

However, closer inspection of the matrices in **Fig. 4A** derived from the WF-Ca^{2+} imaging data, especially at the 12m imaging timepoint, revealed that averaging within *a priori* networks likely obscured a range of differences in connectivity strength between awake and anesthetized mice. Most networks contained nodes showing both increased and decreased connectivity strengths between awake and anesthetized mice which canceled when averaged within network. There were also noticeable differences between awake and anesthetized mice in inter-network connectivity. Some of these features were captured when differences in in brain region connectivity was quantified (**3.4.2**) but further investigation is warranted. In this study, both *a priori* networks, and brain regions (derived from the Allen Atlas), were adopted for the purpose of comparing to the existing literature. In future work, a less constrained approach will be implemented, as we have done previously [13], which will support a more data driven characterization of these features.

4.3 Inter-modal connectivity correlation

The correlation of WF-Ca^{2+} and fMRI connectivity within and between *a priori* networks, separating inter- and intra-hemispheric connections (**Fig. 5**), aligns well with our earlier work (see **Fig. 6B** in [10]). High inter-modality correlations are recovered within-network in both hemispheres (diagonal, **Fig. 5A**) alongside lower or absent correlations between networks and across hemispheres (off-diagonal, **Fig. 5A**). In our previous work [10], mice were imaged under anesthesia which was suspected as the reason for the lack of inter-hemispheric connectivity agreement between WF-Ca^{2+} and fMRI. In this study, this hypothesis was disproven. Across cortical networks, and imaging timepoints, the same pattern was reproduced regardless of whether mice were anesthetized or awake during imaging, **Fig. 5B**. Further examination of this persistent effect will aim to quantify the role that connection length plays in determining inter-modality connectivity agreement. As in the previous subsection, we anticipate that this analysis will benefit from using a brain atlas comprised of smaller and more similarly sized brain regions.

4.4 Summary of limitations and future directions

The sample size, while sufficient for detecting robust group-level effects, limited some of the analyses that were performed. Specifically, insufficient WF-Ca^{2+} imaging data from anesthetized mice at the 9 and 12m imaging timepoints as well as no group that underwent Phase-one: “Initial Progressive Training” prior to the 12m imaging timepoint (which prevented a definitive demonstration that Phase-two: “Refresher Training” was responsible for reducing subject motion). Future studies will provide these answers alongside a more comprehensive characterization of acute and chronic stress. Additional analyses, which will be supported by an increased cohort size, will include a more in-depth characterization of inter-network connectivity, the role of connection length in inter-modality connectivity agreement, as well as analyses of dynamic connectivity [1,4,18,68].

5. Conclusions

This work introduces longitudinal, simultaneous WF-Ca^{2+} and fMRI in awake mice, yielding high-quality, reproducible multimodal data. Novel aspects of cortex-wide patterned activity in awake mice were captured. Convergent and divergent activity patterns in awake and anesthetized animals were quantified and compared across imaging timepoints and modalities. This work sets the stage for future studies in awake mice, where a wider spectrum of behaviors and brain states can be examined in healthy animals and models of disease.

Acknowledgments

Drs. Joel Greenwood and Omer Mano from Neurotechnology Core and Dr. Peter Brown from Magnetic Resonance Research Center Yale University for their technological expertise. Dr. Joanes Grandjean for critical discussion. Dr. Yonghyun Ha for hardware support. CH was supported by NIH R25MH119043. EMRL, FM, SMS were supported by NIH R01 NS130069-01.

Author contributions

Conceptualization: FM, SMS, EMRL. Methodology: FM, XS, TK, CH, EMRL. Investigation: FM, EMRL. Visualization: FM, EMRL. Funding acquisition: SMS, EMRL. Project administration: FM, EMRL. Supervision: EMRL. Writing—original draft: FM. Writing—review & editing: all co-authors.

Declaration of interests

XP owns small stakes in Veridat and Tytonix which are tech startup companies.

References

1 van den Heuvel, M. P. & Hulshoff Pol, H. E. Exploring the brain network: a review on resting-state fMRI functional connectivity. *Eur Neuropsychopharmacol* **20**, 519-534 (2010). https://doi.org/10.1016/j.euroneuro.2010.03.008

2 Sheline, Y. I. & Raichle, M. E. Resting state functional connectivity in preclinical Alzheimer's disease. *Biol Psychiatry* **74**, 340-347 (2013). https://doi.org/10.1016/j.biopsych.2012.11.028

3 Van Essen, D. C. *et al.* The Human Connectome Project: a data acquisition perspective. *Neuroimage* **62**, 2222-2231 (2012). https://doi.org/10.1016/j.neuroimage.2012.02.018

4 Xu, N. *et al.* Functional Connectivity of the Brain Across Rodents and Humans. *Front Neurosci* **16**, 816331 (2022). https://doi.org/10.3389/fnins.2022.816331

5 Pagani, M., Gutierrez-Barragan, D., de Guzman, A. E., Xu, T. & Gozzi, A. Mapping and comparing fMRI connectivity networks across species. *Commun Biol* **6**, 1238 (2023). https://doi.org/10.1038/s42003-023-05629-w

6 Mandino, F. *et al.* A triple-network organization for the mouse brain. *Mol Psychiatry* **27**, 865-872 (2022). https://doi.org/10.1038/s41380-021-01298-5

7 Mandino, F. *et al.* Animal Functional Magnetic Resonance Imaging: Trends and Path Toward Standardization. *Front Neuroinform* **13**, 78 (2019). https://doi.org/10.3389/fninf.2019.00078

8 Logothetis, N. K. & Pfeuffer, J. On the nature of the BOLD fMRI contrast mechanism. *Magn Reson Imaging* **22**, 1517-1531 (2004). https://doi.org/10.1016/j.mri.2004.10.018

9 Lake, E. M. R. & Higley, M. J. Building bridges: simultaneous multimodal neuroimaging approaches for exploring the organization of brain networks. *Neurophotonics* **9**, 032202 (2022). https://doi.org/10.1117/1.NPh.9.3.032202

10 Lake, E. M. R. *et al.* Simultaneous cortex-wide fluorescence Ca(2+) imaging and whole-brain fMRI. *Nat Methods* **17**, 1262-1271 (2020). https://doi.org/10.1038/s41592-020-00984-6

11 Cardin, J. A., Crair, M. C. & Higley, M. J. Mesoscopic Imaging: Shining a Wide Light on Large-Scale Neural Dynamics. *Neuron* **108**, 33-43 (2020). https://doi.org/10.1016/j.neuron.2020.09.031

12 Barson, D. *et al.* Simultaneous mesoscopic and two-photon imaging of neuronal activity in cortical circuits. *Nat Methods* **17**, 107-113 (2020). https://doi.org/10.1038/s41592-019-0625-2

13 Vafaii, H. *et al.* Multimodal measures of spontaneous brain activity reveal both common and divergent patterns of cortical functional organization. *Nat Commun* **15**, 229 (2024). https://doi.org/10.1038/s41467-023-44363-z

14 O'Connor, D. *et al.* Functional network properties derived from wide-field calcium imaging differ with wakefulness and across cell type. *Neuroimage* **264**, 119735 (2022). https://doi.org/10.1016/j.neuroimage.2022.119735

15 Mandino, F. *et al.* Multimodal identification of the mouse brain using simultaneous Ca(2+) imaging and fMRI. *Commun Biol* **8**, 665 (2025). https://doi.org/10.1038/s42003-025-08037-4

16 Mandino, F., Vujic, S., Grandjean, J. & Lake, E. M. R. Where do we stand on fMRI in awake mice? *Cereb Cortex* **34** (2024). https://doi.org/10.1093/cercor/bhad478

17 Fadel, L. C. *et al.* A Mouse Holder for Awake Functional Imaging in Unanesthetized Mice: Applications in (31)P Spectroscopy, Manganese-Enhanced Magnetic Resonance Imaging Studies, and Resting-State Functional Magnetic Resonance Imaging. *Biosensors (Basel)* **12** (2022). https://doi.org/10.3390/bios12080616

18 Gutierrez-Barragan, D. *et al.* Unique spatiotemporal fMRI dynamics in the awake mouse brain. *Curr Biol* **32**, 631-644 e636 (2022). https://doi.org/10.1016/j.cub.2021.12.015

19 Dinh, T. N. A., Jung, W. B., Shim, H. J. & Kim, S. G. Characteristics of fMRI responses to visual stimulation in anesthetized vs. awake mice. *Neuroimage* **226**, 117542 (2021). https://doi.org/10.1016/j.neuroimage.2020.117542

20 Tsurugizawa, T. & Yoshimaru, D. Impact of anesthesia on static and dynamic functional connectivity in mice. *Neuroimage* **241**, 118413 (2021). https://doi.org/10.1016/j.neuroimage.2021.118413

21 Cramer, S. W. *et al.* Wide-field calcium imaging reveals widespread changes in cortical functional connectivity following mild traumatic brain injury in the mouse. *Neurobiol Dis* **176**, 105943 (2023). https://doi.org/10.1016/j.nbd.2022.105943

22 Zhao, H. T. *et al.* Neurovascular dynamics of repeated cortical spreading depolarizations after acute brain injury. *Cell Rep* **37**, 109794 (2021). https://doi.org/10.1016/j.celrep.2021.109794

23 Ren, C. & Komiyama, T. Characterizing Cortex-Wide Dynamics with Wide-Field Calcium Imaging. *J Neurosci* **41**, 4160-4168 (2021). https://doi.org/10.1523/JNEUROSCI.3003-20.2021

24 Greene, A. S., Horien, C., Barson, D., Scheinost, D. & Constable, R. T. Why is everyone talking about brain state? *Trends Neurosci* **46**, 508-524 (2023). https://doi.org/10.1016/j.tins.2023.04.001

25 Lake, E. M. R. Consciousness: Mapping the awake mouse brain. *Curr Biol* **32**, R138-R140 (2022). https://doi.org/10.1016/j.cub.2021.11.033

26 Grandjean, J., Schroeter, A., Batata, I. & Rudin, M. Optimization of anesthesia protocol for resting-state fMRI in mice based on differential effects of anesthetics on functional connectivity patterns. *Neuroimage* **102**, 838-847 (2014). https://doi.org/10.1016/j.neuroimage.2014.08.043

27 Slupe, A. M. & Kirsch, J. R. Effects of anesthesia on cerebral blood flow, metabolism, and neuroprotection. *J Cereb Blood Flow Metab* **38**, 2192-2208 (2018). https://doi.org/10.1177/0271678X18789273

28 Demertzi, A. *et al.* Human consciousness is supported by dynamic complex patterns of brain signal coordination. *Sci Adv* **5**, eaat7603 (2019). https://doi.org/10.1126/sciadv.aat7603

29 Barttfeld, P. *et al.* Signature of consciousness in the dynamics of resting-state brain activity. *Proc Natl Acad Sci U S A* **112**, 887-892 (2015). https://doi.org/10.1073/pnas.1418031112

30 Reimann, H. M. & Niendorf, T. The (Un)Conscious Mouse as a Model for Human Brain Functions: Key Principles of Anesthesia and Their Impact on Translational Neuroimaging. *Front Syst Neurosci* **14**, 8 (2020). https://doi.org/10.3389/fnsys.2020.00008

31 Grandjean, J. *et al.* A consensus protocol for functional connectivity analysis in the rat brain. *Nat Neurosci* **26**, 673-681 (2023). https://doi.org/10.1038/s41593-023-01286-8

32 Mandino, F. *et al.* Aging-dependent loss of functional connectivity in a mouse model of Alzheimer's disease and reversal by mGluR5 modulator. *Mol Psychiatry* **30**, 1730-1745 (2025). https://doi.org/10.1038/s41380-024-02779-z

33 Hamodi, A. S., Martinez Sabino, A., Fitzgerald, N. D., Moschou, D. & Crair, M. C. Transverse sinus injections drive robust whole-brain expression of transgenes. *Elife* **9** (2020). https://doi.org/10.7554/eLife.53639

34 Chen, T. W. *et al.* Ultrasensitive fluorescent proteins for imaging neuronal activity. *Nature* **499**, 295-300 (2013). https://doi.org/10.1038/nature12354

35 Desrosiers-Grégoire, G., Devenyi, G. A., Grandjean, J. & Chakravarty, M. M. A standardized image processing and data quality platform for rodent fMRI. *Nature Communications* **15**, 6708 (2024).

36 Wang, Q. *et al.* The Allen Mouse Brain Common Coordinate Framework: A 3D Reference Atlas. *Cell* **181**, 936-953 e920 (2020). https://doi.org/10.1016/j.cell.2020.04.007

37 Grandjean, J. *et al.* Common functional networks in the mouse brain revealed by multi-centre resting-state fMRI analysis. *Neuroimage* **205**, 116278 (2020).

38 Wright, P. W. *et al.* Functional connectivity structure of cortical calcium dynamics in anesthetized and awake mice. *PLoS One* **12**, e0185759 (2017). https://doi.org/10.1371/journal.pone.0185759

39 Brier, L. M. *et al.* Separability of calcium slow waves and functional connectivity during wake, sleep, and anesthesia. *Neurophotonics* **6**, 035002 (2019). https://doi.org/10.1117/1.NPh.6.3.035002

40 Laxer, S. *et al.* A non-invasive approach to awake mouse fMRI compatible with multi-modal techniques. *Imaging Neurosci (Camb)* **3** (2025). https://doi.org/10.1162/IMAG.a.920

41 Russo, G., Helluy, X., Behroozi, M. & Manahan-Vaughan, D. Gradual Restraint Habituation for Awake Functional Magnetic Resonance Imaging Combined With a Sparse Imaging Paradigm Reduces Motion Artifacts and Stress Levels in Rodents. *Front Neurosci* **15**, 805679 (2021). https://doi.org/10.3389/fnins.2021.805679

42 Zeng, H., Jiang, Y., Beer-Hammer, S. & Yu, X. Awake Mouse fMRI and Pupillary Recordings in the Ultra-High Magnetic Field. *Front Neurosci* **16**, 886709 (2022). https://doi.org/10.3389/fnins.2022.886709

43 Paasonen, J. *et al.* Multi-band SWIFT enables quiet and artefact-free EEG-fMRI and awake fMRI studies in rat. *Neuroimage* **206**, 116338 (2020). https://doi.org/10.1016/j.neuroimage.2019.116338

44 Mangia, S., Michaeli, S. & Grohn, O. Outlook on zero/ultrashort echo time techniques in functional MRI. *Magn Reson Med* (2025). https://doi.org/10.1002/mrm.70065

45 Gozzi, A. *et al.* Charting the path in rodent functional neuroimaging. *Imaging Neurosci (Camb)* **3** (2025). https://doi.org/10.1162/IMAG.a.12

46 Keilholz, S. D., Pan, W. J., Billings, J., Nezafati, M. & Shakil, S. Noise and non-neuronal contributions to the BOLD signal: applications to and insights from animal studies. *Neuroimage* **154**, 267-281 (2017). https://doi.org/10.1016/j.neuroimage.2016.12.019

47 Zhang, Y. *et al.* Rapid detection of neurons in widefield calcium imaging datasets after training with synthetic data. *Nat Methods* **20**, 747-754 (2023). https://doi.org/10.1038/s41592-023-01838-7

48 Lecoq, J. *et al.* Removing independent noise in systems neuroscience data using DeepInterpolation. *Nat Methods* **18**, 1401-1408 (2021). https://doi.org/10.1038/s41592-021-01285-2

49 Herrera-Portillo, L. *et al.* Whole brain dimensional approach identifies shared and sex-specific networks of stress susceptibility in male and female mice. *bioRxiv*, 2025.2005.2010.653278 (2025). https://doi.org/10.1101/2025.05.10.653278

50 Lupinsky, D. *et al.* Resting-state fMRI reveals altered functional connectivity associated with resilience and susceptibility to chronic social defeat stress in mouse brain. *Mol Psychiatry* **30**, 2943-2954 (2025). https://doi.org/10.1038/s41380-025-02897-2

51 Akil, H. & Nestler, E. J. The neurobiology of stress: Vulnerability, resilience, and major depression. *Proc Natl Acad Sci U S A* **120**, e2312662120 (2023). https://doi.org/10.1073/pnas.2312662120

52 Nietz, A. K. *et al.* Wide-Field Calcium Imaging of Neuronal Network Dynamics In Vivo. *Biology (Basel)* **11** (2022). https://doi.org/10.3390/biology11111601

53 Juczewski, K., Koussa, J. A., Kesner, A. J., Lee, J. O. & Lovinger, D. M. Stress and behavioral correlates in the head-fixed method: stress measurements, habituation dynamics, locomotion, and motor-skill learning in mice. *Sci Rep* **10**, 12245 (2020). https://doi.org/10.1038/s41598-020-69132-6

54 Rynes, M. L. *et al.* Miniaturized head-mounted microscope for whole-cortex mesoscale imaging in freely behaving mice. *Nat Methods* **18**, 417-425 (2021). https://doi.org/10.1038/s41592-021-01104-8

55 Kuti, D. *et al.* The metabolic stress response: Adaptation to acute-, repeated- and chronic challenges in mice. *iScience* **25**, 104693 (2022). https://doi.org/10.1016/j.isci.2022.104693

56 Yoshida, K. *et al.* Physiological effects of a habituation procedure for functional MRI in awake mice using a cryogenic radiofrequency probe. *J Neurosci Methods* **274**, 38-48 (2016). https://doi.org/10.1016/j.jneumeth.2016.09.013

57 Tsurugizawa, T. *et al.* Awake functional MRI detects neural circuit dysfunction in a mouse model of autism. *Sci Adv* **6**, eaav4520 (2020). https://doi.org/10.1126/sciadv.aav4520

58 Popp, J. L. *et al.* Structural-functional brain network coupling during cognitive demand reveals intelligence-relevant communication strategies. *Commun Biol* **8**, 855 (2025). https://doi.org/10.1038/s42003-025-08231-4

59 Fotiadis, P. *et al.* Structure-function coupling in macroscale human brain networks. *Nat Rev Neurosci* **25**, 688-704 (2024). https://doi.org/10.1038/s41583-024-00846-6

60 Baum, G. L. *et al.* Development of structure-function coupling in human brain networks during youth. *Proc Natl Acad Sci U S A* **117**, 771-778 (2020). https://doi.org/10.1073/pnas.1912034117

61 Grandjean, J., Zerbi, V., Balsters, J. H., Wenderoth, N. & Rudin, M. Structural Basis of Large-Scale Functional Connectivity in the Mouse. *J Neurosci* **37**, 8092-8101 (2017). https://doi.org/10.1523/JNEUROSCI.0438-17.2017

62 Melozzi, F. *et al.* Individual structural features constrain the mouse functional connectome. *Proc Natl Acad Sci U S A* **116**, 26961-26969 (2019). https://doi.org/10.1073/pnas.1906694116

63 Benozzo, D. *et al.* Macroscale coupling between structural and effective connectivity in the mouse brain. *Sci Rep* **14**, 3142 (2024). https://doi.org/10.1038/s41598-024-51613-7

64 Dvorakova, L. *et al.* Whole-brain responses to visual and auditory stimuli in anesthetized and minimally restrained awake mice using quiet zero echo time fMRI. *Imaging Neurosci (Camb)* **2** (2024). https://doi.org/10.1162/imag_a_00384

65 Paasonen, J., Stenroos, P., Salo, R. A., Kiviniemi, V. & Grohn, O. Functional connectivity under six anesthesia protocols and the awake condition in rat brain. *Neuroimage* **172**, 9-20 (2018). https://doi.org/10.1016/j.neuroimage.2018.01.014

66 Desai, M. *et al.* Mapping brain networks in awake mice using combined optical neural control and fMRI. *J Neurophysiol* **105**, 1393-1405 (2011). https://doi.org/10.1152/jn.00828.2010

67 Jonckers, E. *et al.* Different anesthesia regimes modulate the functional connectivity outcome in mice. *Magn Reson Med* **72**, 1103-1112 (2014). https://doi.org/10.1002/mrm.24990

68 Xu, N. *et al.* QPPLab: A generally applicable software package for detecting, analyzing, and visualizing large-scale quasiperiodic spatiotemporal patterns (QPPs) of brain activity. *bioRxiv* (2023). https://doi.org/10.1101/2023.09.25.559086